

Tangent space Krylov computation of real-frequency spectral functions: Influence of density-assisted hopping on 2D Mott physics

Oleksandra Kovalska,¹ Jan von Delft,¹ and Andreas Gleis²

¹*Arnold Sommerfeld Center for Theoretical Physics, Center for NanoScience, and Munich Center for Quantum Science and Technology, Ludwig-Maximilians-Universität München, 80333 Munich, Germany*

²*Department of Physics and Astronomy, Rutgers University, Piscataway, NJ 08854, USA*

(Dated: October 9, 2025)

We present a tangent-space Krylov (TaSK) method for efficient computation of zero-temperature real-frequency spectral functions on top of ground state (GS) matrix product states (MPS) obtained from the Density Matrix Renormalization Group. It relies on projecting resolvents to the tangent space of the GS-MPS, where they can be efficiently represented using Krylov space techniques. This allows for a direct computation of spectral weights and their corresponding positions on the real-frequency axis. We demonstrate the accuracy and efficiency of the TaSK approach by showcasing spectral data for various models. These include the 1D Haldane-Shastry and Heisenberg models as benchmarks. As an interesting application, we study the Hubbard model on a cylinder at half-filling, augmented by a density-assisted hopping (DAH) term. We find that DAH leads to particle-hole asymmetric single-particle mobilities and lifetimes in the resulting Mott insulator, and identify the responsible scattering processes. Further, we find that DAH influences the dispersion of Green's function zeros beyond its range, which has a frustrating effect on the Mott insulator studied here.

DOI:

Introduction.— Numerical methods based on matrix product states (MPS) form a robust toolbox for studying strongly correlated systems, a prime example being the density matrix renormalization group (DMRG) [1, 2]. Although DMRG has become a staple for ground-state searches, extending its success to dynamical correlation functions remains at the current frontier of research. In this area, the existing approaches follow two distinct strategies: one relies on time evolution and a subsequent Fourier transform [3–7]. Its main limitation is the inevitable growth of entanglement, making it difficult to reach very long times or correspondingly low frequencies. The other strategy aims to compute dynamical quantities directly in frequency space [8–16].

One of the earliest frequency-space ideas, introduced by Hallberg [17], employed a Lanczos-based [18] continued fraction expansion. It motivated further work [19–22] on formulating a Lanczos scheme in the MPS context – a task that proves challenging due to structural limitations. The core steps of any Lanczos implementation are the application of the Hamiltonian to a quantum state and its subsequent orthogonalization against other states. In the MPS framework, these operations increase the bond dimension and leave the manifold of MPSs of fixed bond dimension, which lacks a vector-space structure. To keep the computational cost manageable, they must therefore be followed by compression. This introduces truncation errors that accumulate over iterations, leading to a global loss of orthogonality and convergence issues. These can be mitigated by reorthogonalization [20] or restarting procedures [21].

In this Letter, we introduce a novel tangent-space Krylov (TaSK) method, which restricts computations

to the *tangent space* of the MPS manifold at the ground state, instead of the MPS manifold itself. Since the former has a vector-space structure, it enables us to formulate a Lanczos scheme devoid of orthogonality issues. Our approach uses a direct finite-size MPS adaptation [23, 24] of the quasiparticle ansatz [25–31], which has been successfully employed to compute spectral functions on top of uniform MPSs. We further establish the 2-site energy variance [24, 32] as a novel means to estimate the projection errors due to the tangent space restriction.

We benchmark TaSK on the Haldane-Shastry and Heisenberg chains, finding excellent agreement with analytical results for the dynamical structure factor. As a challenging application offering new physical insight, we consider the Hubbard model on a cylinder, augmented by a density-assisted hopping (DAH) term [33–43]. The spectral functions and self-energies obtained for the Mott insulating phase exhibit strong particle-hole asymmetry, which is absent in a Hartree-Fock treatment of DAH. We identify scattering processes causing the mobility and lifetime asymmetries and find an emergent next-nearest neighbor contribution to the Mott-pole dispersion.

Method.— Consider a Hamiltonian H of an \mathcal{L} -site system, represented as a matrix product operator (MPO)

$$H = \star \begin{array}{c} W_1 \\ \square \\ \vdots \\ W_2 \end{array} \text{---} \begin{array}{c} \square \\ \vdots \\ \square \end{array} \text{---} \begin{array}{c} W_\ell \\ \square \\ \vdots \\ w \\ \square \\ \vdots \\ W_{\mathcal{L}-1} \\ \square \\ \vdots \\ W_{\mathcal{L}} \end{array} \star. \quad (1)$$

Here, d denotes the dimension of the local Hilbert space and w the dimension of the internal virtual bond. Its ground state wavefunction Ψ_g , obtained through DMRG, can be expressed in site-canonical MPS form as

$$\Psi_g = \star \begin{array}{c} A_1 \\ \square \\ \vdots \\ A_{\ell-1} \\ \square \\ \vdots \\ C_\ell \\ \square \\ \vdots \\ B_{\ell+1} \\ \square \\ \vdots \\ B_{\mathcal{L}} \end{array} \text{---} \begin{array}{c} \square \\ \vdots \\ \square \end{array} \star, \quad (2)$$

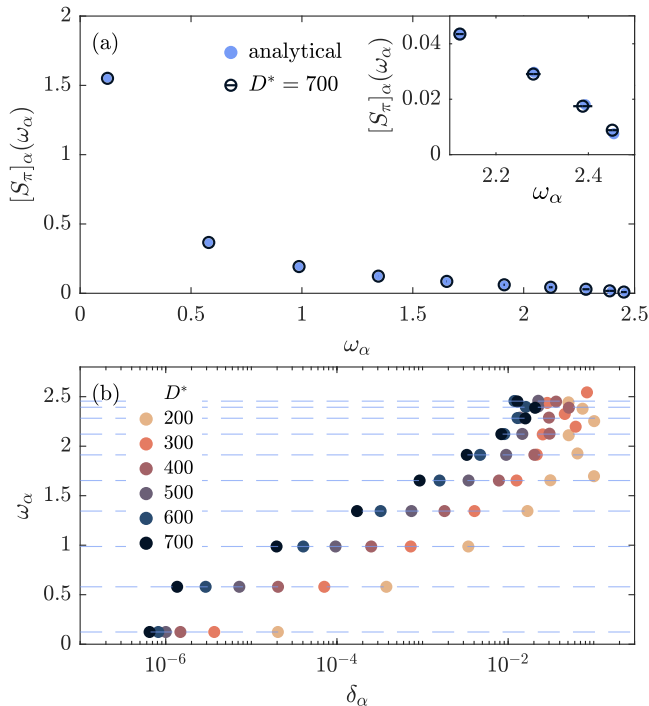


FIG. 1. Dynamical structure factor of the $\mathcal{L} = 40$ Haldane-Shastry model at $k = \pi$ and $\mathcal{N}_{\text{kr}} = 30$. (a) Comparison between analytical values (blue dots) and the TaSK result (black circles) for $D^* = 700$. Horizontal bars depict δ_α as error estimate for ω_α . Inset: zoom to high frequencies. (b) Convergence trend across data sets with increasing D^* , relative to δ_α . Dashed lines indicate the analytical values from (a).

Next, we benchmark TaSK for the antiferromagnetic spin- $\frac{1}{2}$ Heisenberg chain $H_{\text{Heis}} = \sum_{\ell=1}^{\mathcal{L}-1} \mathbf{S}_\ell \cdot \mathbf{S}_{\ell+1}$. In contrast to the HSM, the spinons in this model interact, leading to multi-spin contributions in $S_k(\omega)$ ($\sim 27\%$ of the total spectral weight [60]) and a broad distribution of spectral weight over the entire frequency range. This poses a particular challenge for Lanczos-based methods [8, 17, 20] as each new peak requires an additional iteration.

In Fig. 2 we present $S_\pi(\omega)$ computed for $\mathcal{L} = 64$ and $\mathcal{L} = 128$ and compared with Bethe ansatz results [60] in the thermodynamic limit. For both system sizes, we keep $D^* = 512$ SU(2) multiplets and define the spin-wave operator S_k^z as above. To approximate $S_\pi(\omega)$ in the thermodynamic limit, the two data sets of discrete frequencies ω_α are collapsed onto a single curve using the rescaling scheme described in Sec. IV (D) of Ref. 11 after preliminary binning (see Sec. S-3 of Ref. 45). The resulting data points closely follow the Bethe-ansatz curve corresponding to the full 2 + 4-spinon contribution.

Density-assisted hopping in the 2D Hubbard model.— Due to its efficiency, TaSK can readily obtain spectra of interacting electrons on a 10×4 cylinder, where ground-state calculations are already challenging. Our goal is to study how density-assisted hopping (DAH) influences the physics of the 2D Hubbard model at half-filling, where it describes a Mott insulator—the parent system from

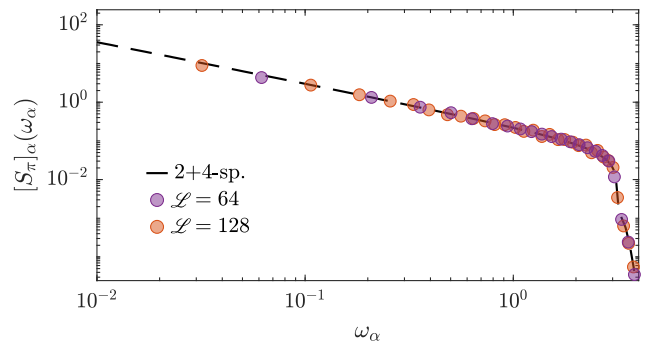


FIG. 2. Dynamical structure factor of the Heisenberg chain at $k = \pi$. The dashed line indicates the exact Bethe ansatz result for the full 2 + 4-spinon contribution from Ref. 60.

which superconductivity arises upon doping. Hirsch has argued that DAH is pivotal for high- T_c superconductivity in cuprates [33, 34], and understanding its physical consequences is an active area of research [35–43].

A recent DMRG-based downfolding study of the Emery model [42] yielded a single-band Hubbard model augmented by a DAH term, $H = H_{t-U} + H_n$, with

$$H_{t-U} = -t \sum_{\langle ij \rangle, \sigma} (c_{i\sigma}^\dagger c_{j\sigma} + \text{h.c.}) + U \sum_i n_{i\uparrow} n_{i\downarrow}, \quad (11a)$$

$$H_n = -t_n \sum_{\langle ij \rangle, \sigma} (c_{i\sigma}^\dagger c_{j\sigma} + \text{h.c.}) (n_{i\bar{\sigma}} + n_{j\bar{\sigma}}). \quad (11b)$$

Here, $c_{i\sigma}^\dagger$ is a hole creation operator, $n_{i\sigma} = c_{i\sigma}^\dagger c_{i\sigma}$ the hole-number operator, $\bar{\sigma}$ denotes the spin projection opposite to σ , and $\langle ij \rangle$ denotes nearest neighbors. The DAH hopping rate was found [42] to be substantial, $t_n \simeq 0.6t$, significantly enhancing hole mobility *and* pairing. The latter finding cannot be understood within a simple Hartree-Fock (HF) treatment of DAH, which effectively replaces t by $t_{\text{eff}} = t + 2t_n \langle n_{\bar{\sigma}} \rangle$, thereby remaining a pure Hubbard model that does not exhibit superconductivity [61].

Here, we use TaSK to examine the (beyond-HF) effects of DAH on the single-particle spectral function, $A_{\mathbf{k}}(\omega) = S[c_{\mathbf{k}\sigma}^\dagger](\omega) + S[c_{\mathbf{k}\sigma}](\omega)$, of the half-filled Mott insulator. We find a surprisingly strong particle-hole asymmetry in $A_{\mathbf{k}}(\omega)$ and a next-nearest neighbor contribution to the dispersion of the self-energy pole.

We study the model (11) on a half-filled 10×4 cylinder, with $U = 12.6$ and either $t = 1.68$, $t_n = 0$ (denoted “ $t-U$ ”) or $t = 1$, $t_n = 0.6$ (denoted “ $t-t_n-U$ ”), matching the parameters of Fig. 4 of Ref. 42. (For $t-t_n-U$, a HF treatment of DAH yields $t_{\text{eff}} = 1.6$, similar to t for $t-U$.) We keep at least $D^* = 2000$ U(1) \times SU(2) multiplets. Figures 3(a,c) show $A_{\mathbf{k}}(\omega)$ for the Mott insulators obtained for $t-U$ or $t-t_n-U$, respectively, and Figs. 3(b,d) the imaginary parts of the corresponding self-energies $\Sigma_{\mathbf{k}}(\omega)$. Our broadening scheme and TaSK convergence properties are discussed in Secs. S-2 and S-3 of the SM [45], respectively.

For $t-U$, $A_{\mathbf{k}}(\omega)$ [Fig. 3(a)] exhibits a Mott gap of size $6.67 < U$. Apart from broad incoherent features, the Hubbard bands exhibit dispersive coherent features, in

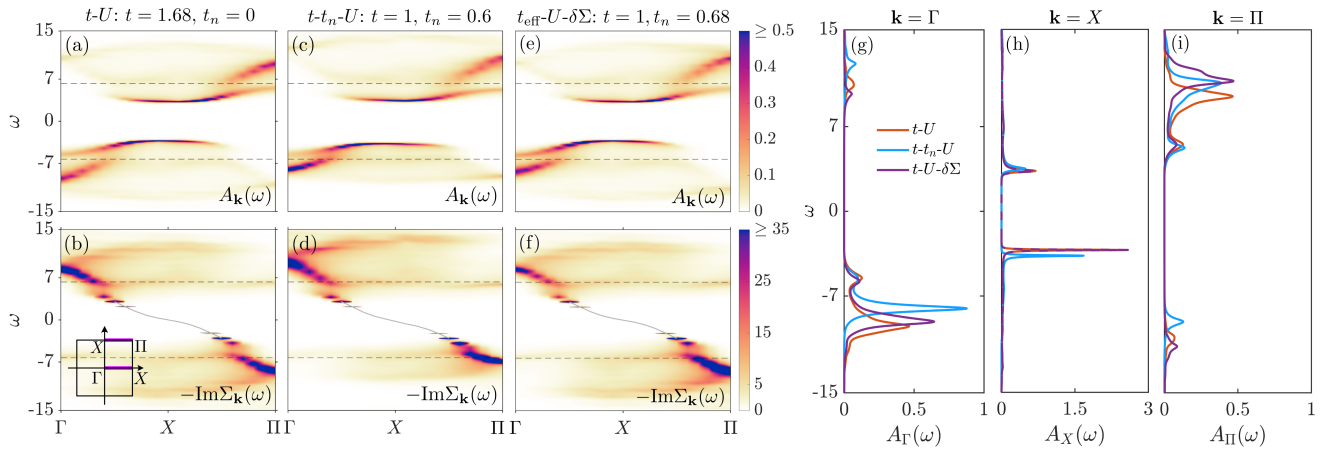


FIG. 3. Comparison of $A_{\mathbf{k}}(\omega)$ and $-\text{Im}\Sigma_{\mathbf{k}}(\omega)$ for the Hubbard model on a 10×4 cylinder, computed via TaSK (a, b) without and (c, d) with DAH, and (e, f) computed by treating DAH simplistically via Eq. (12). Solid gray lines in (b, d, f) mark the self-energy pole where it becomes too sharp for the frequency resolution of our grid. Dashed gray lines indicate $\omega = \pm U/2$. Inset in (b): purple lines show the Brillouin zone paths $\Gamma \rightarrow X$ and $X \rightarrow \Pi$. (g, h, i) Line cuts of $A_{\mathbf{k}}(\omega)$ for $\mathbf{k} = \Gamma, X, \Pi$.

particular at their inner edges. The self-energy [Fig. 3(b)] has a characteristic S -shaped spectrum [62], exhibiting broad horizontal bands connected by a sharp, dispersive pole. Both $A_{\mathbf{k}}(\omega)$ and $\text{Im}\Sigma_{\mathbf{k}}(\omega)$ are particle-hole symmetric, as expected, i.e. invariant under $\omega \rightarrow -\omega$, $\mathbf{k} \rightarrow \mathbf{k} + \mathbf{\Pi}$, where $\mathbf{\Pi} = (\pi, \pi)$.

For $t-t_n-U$, the corresponding results are shown in Figs. 3(c, d). The overall features are similar to those of $t-U$, but t_n , though small ($t_n < 0.05 U$), introduces a significant particle-hole asymmetry [see also Figs. 3(g-i)], a dynamical effect that goes beyond HF. In particular, the particle part ($\omega < 0$) of $A_{\mathbf{k}}(\omega)$ is more coherent, i.e. dispersive features are sharper and exhibit smaller decay rates, and conversely for the hole spectrum ($\omega > 0$). $\text{Im}\Sigma_{\mathbf{k}}(\omega)$ shows corresponding weight redistributions. Moreover, the effective bandwidth is reduced or increased for particle or hole excitations, respectively, i.e. spectral features at $\omega < 0$ or > 0 are “squeezed” or “stretched” in ω . Thus, t_n dynamically enhances hole mobility compared to particle mobility (an effect also reported in Ref. 42), while hole lifetimes are reduced compared to particle lifetimes.

Which scattering events generate the particle-hole asymmetric features? A perturbative expansion of $\Sigma_{\mathbf{k}}(\omega)$ in t_n and U shows that at second order, they arise from *mixed* t_n-U scattering (see Sec. S-5 of SM [45]): a propagating particle or hole emits a particle-hole pair via the t_n vertex and reabsorbs it via the U vertex, or vice versa. Using this insight, and the fact that the U vertex and part of the t_n vertex do not depend on transfer momenta, we can estimate the latter’s contribution to the DAH-induced change in the self-energy, $\delta\Sigma_{\mathbf{k}}^{t_n}$, as follows (see Sec. S-6 of SM [45]): We use TaSK to compute the self-energy of the $t-U$ Hubbard model with hopping t_{eff} , denoted $\Sigma_{\mathbf{k}}^{t_{\text{eff}}-U}$; from the latter, we obtain $\delta\Sigma_{\mathbf{k}}^{t_n}$ by replacing either the initial or final U vertex by the transfer-momentum-independent

part of the t_n vertex. This yields

$$\delta\Sigma_{\mathbf{k}}^{t_n}(\omega) = -4 \frac{t_n \gamma_{\mathbf{k}}}{U} (\Sigma_{\mathbf{k}}^{t_{\text{eff}}-U}(\omega) - \Sigma_{\mathbf{k}}^{\text{HF}}), \quad (12)$$

where $\gamma_{\mathbf{k}} = \cos k_x + \cos k_y$ and $\Sigma_{\mathbf{k}}^{\text{HF}}$ is the HF self-energy. This “ $t_{\text{eff}}-U-\delta\Sigma$ ” scheme yields a total self-energy of $\Sigma_{\mathbf{k}}^{t_{\text{eff}}-U}(\omega) + \delta\Sigma_{\mathbf{k}}^{t_n}(\omega)$. It is shown in Fig. 3(f), computed using $t_{\text{eff}} = t + t_n = 1 + 0.68$ (so that $\Sigma_{\mathbf{k}}^{t_{\text{eff}}-U}(\omega)$ equals $\Sigma_{\mathbf{k}}(\omega)$ of Fig. 3(b)), almost matching the $t-t_n-U$ settings of Fig. 3(d) (where $t_{\text{eff}} = 1 + 0.6$). The corresponding $t_{\text{eff}}-U-\delta\Sigma$ spectral function [Fig. 3(e)] indeed reproduces several properties of the coherent features of $t-t_n-U$ in Fig. 3(c): reduced effective bandwidth and decay rate for particle excitations, and vice versa for hole excitations [see also Figs. 3(g-i)]. By contrast, $\delta\Sigma^{t_n}$ hardly affects the incoherent background; reproducing the latter’s $t-t_n-U$ properties thus requires a more elaborate treatment.

A hallmark feature of Mott insulators is their self-energy poles [grey lines in Figs. 3(b, d)], which cause Green’s function zeros. Their generically dispersive nature, which has only recently been fully appreciated [50], is currently under active investigation, with interesting results ranging from topology [50, 63–67] to possible connections to spinon physics [68–71]. If the interaction is purely Hubbard, it can be shown that the pole dispersion is directly inherited from the non-interacting dispersion [50].

Thus, for $t-U$, the Mott pole dispersion $\xi_{\mathbf{k}}$ should contain only nearest-neighbor terms. Indeed, using the ansatz $\xi_{\mathbf{k}} = -2\tau(\cos k_x + \cos k_y) - 4\tau' \cos k_x \cos k_y$ [72], where τ and τ' are nearest and next-nearest neighbor amplitudes, we obtain a good fit with $\tau \simeq -2.03$ and $\tau' = 0$, confirming this expectation (see Sec. S-7 C of SM [45]). By contrast, for $t-t_n-U$ we find $\tau \simeq -1.86$ and $\tau' \simeq 0.17$. Hence *nearest-neighbor* DAH generates a sizeable *next-nearest neighbor* term τ' —a remarkable result, arising from the fact that the DAH t_n vertex, unlike the U vertex, delocalizes electrons beyond single-particle hopping and

HF (see Sec. S-7 of the SM [45]). This emergence of non-zero τ' suggests that t_n may have a similar frustration effect as the much-studied next-nearest neighbor hopping t' for the t - t' Hubbard model, in particular if $\xi_{\mathbf{k}}$ can be interpreted as a spinon dispersion. Since frustration from t' can stabilize superconductivity in the Hubbard model [73, 74], a similar effect from t_n may, together with the previously discussed mobility and lifetime effects, stabilize superconductivity in the t - t_n Hubbard model [42].

Outlook.— We showed that TaSK is an efficient and accurate method for computing real-frequency spectral functions. Its main source of error comes from the projection to the tangent space and can be estimated via the introduced two-site variance. Due to its relatively light-weight nature, it is especially useful in cases where ground-state calculations are already challenging. These include strongly correlated electron systems on cylinders, geared, for instance, towards cuprates [75–78], heavy-fermions [79–86], Moiré systems [87–89], or systems with strong electron-boson couplings [90–93].

As a first step in this direction, we have applied TaSK to a Hubbard cylinder exhibiting DAH, a problem relevant to cuprates. Our finding that mixed t_n - U scattering leads to enhanced hole mobilities and a possibly frustrating next-nearest neighbor contribution to the dispersion of the self-energy pole may be relevant for high- T_c superconductivity. A more detailed study of this, which would include doping and the calculation of other dynamical properties such as spin or pair spectra, is left for future work.

Acknowledgments.— We thank Seung-Sup Lee, Sebastian Pöckel, Felipe Picoli, Dai-Wei Qu, and Steven White for helpful discussions, and Jean-Sébastien Caux on providing the Bethe-ansatz data in Fig. 2. This work was supported in part by the Deutsche Forschungsgemeinschaft under grants INST 86/1885-1 FUGG, LE 3883/2-2 and Germany’s Excellence Strategy EXC-2111 (Project No. 390814868). It is part of the Munich Quantum Valley, supported by the Bavarian state government with funds from the Hightech Agenda Bayern Plus. The National Science Foundation supported JvD in part under PHY-1748958. AG acknowledges support from the Abrahams Postdoctoral Fellowship of the Center for Materials Theory at Rutgers University.

-
- [1] S. R. White, Density matrix formulation for quantum renormalization groups, *Phys. Rev. Lett.* **69**, 2863 (1992).
- [2] U. Schollwöck, The density-matrix renormalization group in the age of matrix product states, *Annals of Physics* **326**, 96 (2011).
- [3] G. Vidal, Efficient simulation of one-dimensional quantum many-body systems, *Phys. Rev. Lett.* **93**, 040502 (2004).
- [4] S. R. White and A. E. Feiguin, Real-time evolution using the density matrix renormalization group, *Phys. Rev. Lett.* **93**, 076401 (2004).
- [5] A. J. Daley, C. Kollath, U. Schollwöck, and G. Vidal, Time-dependent density-matrix renormalization-group using adaptive effective Hilbert spaces, *Journal of Statistical Mechanics: Theory and Experiment* **2004**, P04005.
- [6] S. Paeckel, T. Köhler, A. Swoboda, S. R. Manmana, U. Schollwöck, and C. Hubig, Time-evolution methods for matrix-product states, *Annals of Physics* **411**, 167998 (2019).
- [7] M. Grundner, P. Westhoff, F. B. Kugler, O. Parcollet, and U. Schollwöck, Complex time evolution in tensor networks and time-dependent Green’s functions, *Phys. Rev. B* **109**, 155124 (2024).
- [8] T. D. Kühner and S. R. White, Dynamical correlation functions using the density matrix renormalization group, *Phys. Rev. B* **60**, 335 (1999).
- [9] E. Jeckelmann, Dynamical density-matrix renormalization-group method, *Phys. Rev. B* **66**, 045114 (2002).
- [10] C. Raas and G. S. Uhrig, Spectral densities from dynamic density-matrix renormalization, *Eur. Phys. J. B* **45**, 293 (2005).
- [11] A. Holzner, A. Weichselbaum, I. P. McCulloch, U. Schollwöck, and J. von Delft, Chebyshev matrix product state approach for spectral functions, *Phys. Rev. B* **83**, 195115 (2011).
- [12] F. A. Wolf, I. P. McCulloch, O. Parcollet, and U. Schollwöck, Chebyshev matrix product state impurity solver for dynamical mean-field theory, *Phys. Rev. B* **90**, 115124 (2014).
- [13] F. A. Wolf, J. A. Justiniano, I. P. McCulloch, and U. Schollwöck, Spectral functions and time evolution from the Chebyshev recursion, *Phys. Rev. B* **91**, 115144 (2015).
- [14] A. Nocera and G. Alvarez, Spectral functions with the density matrix renormalization group: Krylov-space approach for correction vectors, *Phys. Rev. E* **94**, 053308 (2016).
- [15] A. Nocera and G. Alvarez, Root- N Krylov-space correction vectors for spectral functions with the density matrix renormalization group, *Phys. Rev. B* **106**, 205106 (2022).
- [16] S. Paeckel, Spectral decomposition and high-accuracy Greens functions: Overcoming the Nyquist-Shannon limit via complex-time Krylov expansion (2025), arXiv:2411.09680 [cond-mat.str-el].
- [17] K. A. Hallberg, Density-matrix algorithm for the calculation of dynamical properties of low-dimensional systems, *Phys. Rev. B* **52**, R9827 (1995).
- [18] E. Koch, The Lanczos method, in *The LDA+DMFT Approach to Strongly Correlated Materials*, Modeling and Simulation, Vol. 1, edited by E. Pavarini, E. Koch, D. Vollhardt, and A. Lichtenstein (Forschungszentrum Jülich, Jülich, 2011) pp. 8.1–8.30.
- [19] P. E. Dargel, A. Honecker, R. Peters, R. M. Noack, and T. Pruschke, Adaptive Lanczos-vector method for dynamic properties within the density matrix renormalization group, *Phys. Rev. B* **83**, 161104 (2011).
- [20] P. E. Dargel, A. Wöllert, A. Honecker, I. P. McCulloch, U. Schollwöck, and T. Pruschke, Lanczos algorithm with matrix product states for dynamical correlation functions, *Phys. Rev. B* **85**, 205119 (2012).
- [21] Y. Wang, Z. Yang, and C. B. Mendl, Improved Lanczos algorithm using matrix product states (2025), arXiv:2504.21786 [cond-mat.str-el].
- [22] A. Dektor, P. DelMastro, E. Ye, R. V. Beeumen, and C. Yang, Inexact subspace projection methods for low-

- rank tensor eigenvalue problems (2025), [arXiv:2502.19578](https://arxiv.org/abs/2502.19578) [[math.NA](https://arxiv.org/abs/2502.19578)].
- [23] M. Van Damme, R. Vanhove, J. Haegeman, F. Verstraete, and L. Vanderstraeten, Efficient matrix product state methods for extracting spectral information on rings and cylinders, *Phys. Rev. B* **104**, 115142 (2021).
- [24] A. Gleis, J.-W. Li, and J. von Delft, Projector formalism for kept and discarded spaces of matrix product states, *Phys. Rev. B* **106**, 195138 (2022).
- [25] S. Östlund and S. Rommer, Thermodynamic limit of density matrix renormalization, *Phys. Rev. Lett.* **75**, 3537 (1995).
- [26] S. Rommer and S. Östlund, Class of ansatz wave functions for one-dimensional spin systems and their relation to the density matrix renormalization group, *Phys. Rev. B* **55**, 2164 (1997).
- [27] J. Haegeman, B. Pirvu, D. J. Weir, J. I. Cirac, T. J. Osborne, H. Verschelde, and F. Verstraete, Variational matrix product ansatz for dispersion relations, *Phys. Rev. B* **85**, 100408 (2012).
- [28] J. Haegeman, T. J. Osborne, and F. Verstraete, Post-matrix product state methods: To tangent space and beyond, *Phys. Rev. B* **88**, 075133 (2013).
- [29] J. Haegeman, S. Michalakis, B. Nachtergaele, T. J. Osborne, N. Schuch, and F. Verstraete, Elementary excitations in gapped quantum spin systems, *Phys. Rev. Lett.* **111**, 080401 (2013).
- [30] L. Vanderstraeten, J. Haegeman, and F. Verstraete, Tangent-space methods for uniform matrix product states, *SciPost Phys. Lect. Notes* , 7 (2019).
- [31] W.-L. Tu, H.-K. Wu, N. Schuch, N. Kawashima, and J.-Y. Chen, Generating function for tensor network diagrammatic summation, *Phys. Rev. B* **103**, 205155 (2021).
- [32] C. Hubig, J. Haegeman, and U. Schollwöck, Error estimates for extrapolations with matrix-product states, *Phys. Rev. B* **97**, 045125 (2018).
- [33] J. Hirsch, Bond-charge repulsion and hole superconductivity, *Physica C: Superconductivity and its Applications* **158**, 326 (1989).
- [34] J. Hirsch and F. Marsiglio, Hole superconductivity: Review and some new results, *Physica C: Superconductivity and its Applications* **162-164**, 591 (1989).
- [35] H.-B. Schüttler and A. J. Fedro, Copper-oxygen charge excitations and the effective-single-band theory of cuprate superconductors, *Phys. Rev. B* **45**, 7588 (1992).
- [36] M. Simón, M. Balaña, and A. Aligia, Effective one-band hamiltonian for cuprate superconductor metal-insulator transition, *Physica C: Superconductivity* **206**, 297 (1993).
- [37] A. A. Aligia, K. Hallberg, C. D. Batista, and G. Ortiz, Phase diagrams from topological transitions: The Hubbard chain with correlated hopping, *Phys. Rev. B* **61**, 7883 (2000).
- [38] A. A. Aligia, A. Anfossi, L. Arrachea, C. Degli Esposti Boschi, A. O. Dobry, C. Gazza, A. Montorsi, F. Ortolani, and M. E. Torio, Incommensurability and unconventional superconductor to insulator transition in the Hubbard model with bond-charge interaction, *Phys. Rev. Lett.* **99**, 206401 (2007).
- [39] T. Yang, F.-K. Wen, K. Hao, L.-K. Cao, and R.-H. Yue, The effect of a long-range correlated-hopping interaction on Bariev spin chains, *Entropy* **17**, 6044 (2015).
- [40] M. Zegrodnik and J. Spalek, Universal properties of high-temperature superconductors from real-space pairing: Role of correlated hopping and intersite Coulomb interaction within the t - J - U model, *Phys. Rev. B* **96**, 054511 (2017).
- [41] W. Chen, J. Zhang, and H. Ding, Ground-state instabilities in a Hubbard-type chain with particular correlated hopping at non-half-filling, *Results in Physics* **49**, 106472 (2023).
- [42] S. Jiang, D. J. Scalapino, and S. R. White, Density matrix renormalization group based downfolding of the three-band Hubbard model: Importance of density-assisted hopping, *Phys. Rev. B* **108**, L161111 (2023).
- [43] X. Sun, L. Wang, and H. Ding, Ground-state phase diagram of the unconventional Hubbard chain with bond-charge interaction, *Results in Physics* **64**, 107925 (2024).
- [44] Eigenenergies of the Hamiltonian are extensive, whereas the excitation energy differences probed by $O_{\mathbf{k}}$ are not (our $O_{\mathbf{k}}$ is a superposition of short-ranged operators). To avoid subtractions of large numbers, prone to numerical inaccuracies, we formulate our Lanczos scheme directly for $H - E_{\mathbf{g}}$, implemented by subtracting $E_{\mathbf{g}}/\mathcal{L}$ from the local Hamiltonian on every site.
- [45] See Supplemental Material at [url] for additional information on technical details of TaSK; computation of the error estimates; comparison between spectral data obtained with TaSK and TDVP; convergence and broadening analysis; analytical analysis of density-assisted hopping effects on Mott-insulating physics of the 2D Hubbard model. The Supplemental Material includes Refs. [11, 24, 46–53].
- [46] C. Hubig, I. P. McCulloch, U. Schollwöck, and F. A. Wolf, Strictly single-site DMRG algorithm with subspace expansion, *Phys. Rev. B* **91**, 155115 (2015).
- [47] A. Gleis, J.-W. Li, and J. von Delft, Controlled bond expansion for density matrix renormalization group ground state search at single-site costs, *Phys. Rev. Lett.* **130**, 246402 (2023).
- [48] A. Gleis, J.-W. Li, and J. von Delft, Reply to comment on "controlled bond expansion for density matrix renormalization group ground state search at single-site costs" (2025), [arXiv:2501.12291](https://arxiv.org/abs/2501.12291) [[cond-mat.str-el](https://arxiv.org/abs/2501.12291)].
- [49] W. Dickhoff and C. Barbieri, Self-consistent Green's function method for nuclei and nuclear matter, *Progress in Particle and Nuclear Physics* **52**, 377 (2004).
- [50] N. Wagner, L. Crippa, A. Amaricci, P. Hansmann, M. Klett, E. J. König, T. Schäfer, D. D. Sante, J. Cano, A. J. Millis, A. Georges, and G. Sangiovanni, Mott insulators with boundary zeros, *Nature Communications* **14**, 7531 (2023).
- [51] F. B. Kugler, Improved estimator for numerical renormalization group calculations of the self-energy, *Phys. Rev. B* **105**, 245132 (2022).
- [52] M. Pelz, A. Gleis, and J. von Delft, Liouvillian periodization of the self-energy in cluster dynamical mean-field theories (unpublished).
- [53] V. S. Viswanath and G. Müller, *The Recursion Method* (Springer Berlin, Heidelberg, 1994).
- [54] F. D. M. Haldane and M. R. Zirnbauer, Exact calculation of the ground-state dynamical spin correlation function of a $S=1/2$ antiferromagnetic Heisenberg chain with free spinons, *Phys. Rev. Lett.* **71**, 4055 (1993).
- [55] T. Yamamoto, Y. Saiga, M. Arikawa, and Y. Kuramoto, Exact dynamical structure factor of the degenerate Haldane-Shastry model, *Phys. Rev. Lett.* **84**, 1308 (2000).
- [56] A. Weichselbaum, Non-abelian symmetries in tensor net-

- works: A quantum symmetry space approach, *Annals of Physics* **327**, 2972 (2012).
- [57] A. Weichselbaum, X-symbols for non-Abelian symmetries in tensor networks, *Phys. Rev. Res.* **2**, 023385 (2020).
- [58] A. Weichselbaum, QSpace - An open-source tensor library for Abelian and non-Abelian symmetries, *SciPost Phys. Codebases*, **40** (2024).
- [59] T. Yamamoto, Y. Saiga, M. Arikawa, and Y. Kuramoto, Exact dynamics of the SU(K) Haldane-Shastry model, *Journal of the Physical Society of Japan* **69**, 900 (2000).
- [60] J.-S. Caux and R. Hagemans, The 4-spin dynamical structure factor of the Heisenberg chain, *J. Stat. Mech.* **0612**, P12013 (2006).
- [61] M. Qin, C.-M. Chung, H. Shi, E. Vitali, C. Hubig, U. Schollwöck, S. R. White, and S. Zhang (Simons Collaboration on the Many-Electron Problem), Absence of superconductivity in the pure two-dimensional Hubbard model, *Phys. Rev. X* **10**, 031016 (2020).
- [62] P. Pudliner, T. Schäfer, D. Rost, G. Li, K. Held, and N. Blümer, Momentum structure of the self-energy and its parametrization for the two-dimensional Hubbard model, *Phys. Rev. B* **93**, 195134 (2016).
- [63] C. Setty, F. Xie, S. Sur, L. Chen, M. G. Vergniory, and Q. Si, Electronic properties, correlated topology, and Green's function zeros, *Phys. Rev. Res.* **6**, 033235 (2024).
- [64] N. Wagner, D. Guerci, A. J. Millis, and G. Sangiovanni, Edge zeros and boundary spinons in topological Mott insulators, *Phys. Rev. Lett.* **133**, 126504 (2024).
- [65] S. Bollmann, C. Setty, U. F. P. Seifert, and E. J. König, Topological Green's function zeros in an exactly solved model and beyond, *Phys. Rev. Lett.* **133**, 136504 (2024).
- [66] E. Pangburn, C. Pépin, and A. Banerjee, Topological charge excitations and Green's function zeros in paramagnetic Mott insulators, *Phys. Rev. B* **112**, 085105 (2025).
- [67] E. Pangburn, A. Banerjee, C. Pépin, and C. Bena, Impurity-induced Mott ring states and Mott zeros ring states in the Hubbard operator formalism, *Phys. Rev. B* **112**, 125157 (2025).
- [68] M. Fabrizio, Landau-Fermi liquids without quasiparticles, *Phys. Rev. B* **102**, 155122 (2020).
- [69] J. Skolimowski and M. Fabrizio, Luttinger's theorem in the presence of Luttinger surfaces, *Phys. Rev. B* **106**, 045109 (2022).
- [70] M. Fabrizio, Emergent quasiparticles at Luttinger surfaces, *Nat. Commun.* **13**, 1561 (2022).
- [71] M. Fabrizio, Spin-liquid insulators can be Landau's Fermi liquids, *Phys. Rev. Lett.* **130**, 156702 (2023).
- [72] We obtain the \mathbf{k} -dependent pole by means of a continued fraction expansion of the numerically calculated, discrete self-energy, $\Sigma_{\mathbf{k}}(\omega) = \Sigma_{\mathbf{k}}^{\text{HF}} + \frac{\Delta_{\mathbf{k}}}{\omega - \xi_{\mathbf{k}} + \mathcal{O}(z^{-1})}$. The resulting $\xi_{\mathbf{k}}$ is then fitted with the ansatz in the main text to extract τ and τ' . We have checked that the inclusion of a next-next-nearest neighbor term in our ansatz does not change the fit parameters.
- [73] H. Xu, C.-M. Chung, M. Qin, U. Schollwöck, S. R. White, and S. Zhang, Coexistence of superconductivity with partially filled stripes in the Hubbard model, *Science* **384**, eadh7691 (2024), <https://www.science.org/doi/pdf/10.1126/science.adh7691>.
- [74] C. Zhang, J.-W. Li, D. Nikolaidou, and J. von Delft, Frustration-induced superconductivity in the $t-t'$ Hubbard model, *Phys. Rev. Lett.* **134**, 116502 (2025).
- [75] B. Keimer, S. A. Kivelson, M. R. Norman, S. Uchida, and J. Zaanen, From quantum matter to high-temperature superconductivity in copper oxides, *Nature* **518**, 179 (2015).
- [76] J. P. F. LeBlanc, A. E. Antipov, F. Becca, I. W. Bulik, G. K.-L. Chan, C.-M. Chung, Y. Deng, M. Ferrero, T. M. Henderson, C. A. Jiménez-Hoyos, E. Kozik, X.-W. Liu, A. J. Millis, N. V. Prokof'ev, M. Qin, G. E. Scuseria, H. Shi, B. V. Svistunov, L. F. Tocchio, I. S. Tupitsyn, S. R. White, S. Zhang, B.-X. Zheng, Z. Zhu, and E. Gull (Simons Collaboration on the Many-Electron Problem), Solutions of the two-dimensional Hubbard model: Benchmarks and results from a wide range of numerical algorithms, *Phys. Rev. X* **5**, 041041 (2015).
- [77] S. Jiang, D. J. Scalapino, and S. R. White, Ground-state phase diagram of the $t-t'-J$ model, *Proceedings of the National Academy of Sciences* **118**, e2109978118 (2021).
- [78] Y.-F. Jiang, T. P. Devereaux, and H.-C. Jiang, Ground-state phase diagram and superconductivity of the doped Hubbard model on six-leg square cylinders, *Phys. Rev. B* **109**, 085121 (2024).
- [79] Q. Si, S. Rabello, K. Ingersent, and J. L. Smith, Locally critical quantum phase transitions in strongly correlated metals, *Nature* **413**, 804 (2001).
- [80] P. Coleman, C. Pépin, Q. Si, and R. Ramazashvili, How do Fermi liquids get heavy and die?, *J. Phys. Condens. Matter* **13**, R723 (2001).
- [81] T. Senthil, S. Sachdev, and M. Vojta, Fractionalized Fermi liquids, *Phys. Rev. Lett.* **90**, 216403 (2003).
- [82] B. Danu, Z. Liu, F. F. Assaad, and M. Raczkowski, Zooming in on heavy fermions in Kondo lattice models, *Phys. Rev. B* **104**, 155128 (2021).
- [83] M. Raczkowski, B. Danu, and F. F. Assaad, Breakdown of heavy quasiparticles in a honeycomb Kondo lattice: A quantum Monte Carlo study, *Phys. Rev. B* **106**, L161115 (2022).
- [84] M. Raczkowski and F. F. Assaad, SU(N) Kondo-Heisenberg chain: Phase diagram, Ising criticality, and the coexistence of heavy quasiparticles and valence bond solid order, *Phys. Rev. B* **109**, 205154 (2024).
- [85] A. Gleis, S.-S. B. Lee, G. Kotliar, and J. von Delft, Emergent properties of the periodic Anderson model: A high-resolution, real-frequency study of heavy-fermion quantum criticality, *Phys. Rev. X* **14**, 041036 (2024).
- [86] A. Gleis, S.-S. B. Lee, G. Kotliar, and J. von Delft, Dynamical scaling and Planckian dissipation due to heavy-fermion quantum criticality, *Phys. Rev. Lett.* **134**, 106501 (2025).
- [87] T. Soejima, D. E. Parker, N. Bultinck, J. Hauschild, and M. P. Zaletel, Efficient simulation of Moiré materials using the density matrix renormalization group, *Phys. Rev. B* **102**, 205111 (2020).
- [88] Y. Zhou, D. N. Sheng, and E.-A. Kim, Quantum phases of transition metal dichalcogenide Moiré systems, *Phys. Rev. Lett.* **128**, 157602 (2022).
- [89] S. Chatterjee, M. Ippoliti, and M. P. Zaletel, Skyrmion superconductivity: DMRG evidence for a topological route to superconductivity, *Phys. Rev. B* **106**, 035421 (2022).
- [90] T. Köhler, J. Stolpp, and S. Paeckel, Efficient and flexible approach to simulate low-dimensional quantum lattice models with large local Hilbert spaces, *SciPost Phys.* **10**, 058 (2021).
- [91] J. Sous, M. Chakraborty, R. V. Krems, and M. Berciu, Light bipolarons stabilized by Peierls electron-phonon coupling, *Phys. Rev. Lett.* **121**, 247001 (2018).
- [92] T. Tang, B. Moritz, C. Peng, Z.-X. Shen, and T. P.

- Devereaux, Traces of electron-phonon coupling in one-dimensional cuprates, *Nature Communications* **14**, 3129 (2023).
- [93] L. L. H. Lau, A. Gleis, D. Kaplan, P. Chandra, and P. Coleman, Oscillate and renormalize: Fast phonons reshape the Kondo effect in flat-band systems, *Phys. Rev. B* **111**, 245149 (2025).
- [94] J.-W. Li, A. Gleis, and J. von Delft, Time-dependent variational principle with controlled bond expansion for matrix product states, *Phys. Rev. Lett.* **133**, 026401 (2024).

Supplemental material:
Tangent space Krylov computation of real-frequency spectral functions:
Influence of density-assisted hopping on 2D Mott physics

Oleksandra Kovalska,¹ Jan von Delft,¹ and Andreas Gleis²

¹*Arnold Sommerfeld Center for Theoretical Physics, Center for NanoScience, and Munich Center for Quantum Science and Technology, Ludwig-Maximilians-Universität München, 80333 Munich, Germany*

²*Department of Physics and Astronomy, Rutgers University, Piscataway, NJ 08854, USA*

(Dated: October 9, 2025)

This supplemental material provides additional details and results on the TaSK method, post-processing of discrete data, and theoretical considerations for the 2D Hubbard model with DAH. Section S-1 expands on the technical aspects of the *Method* section in the main text. Section S-2 describes the continued fraction expansion (CFE) broadening scheme used to obtain continuous spectral functions. In Sec. S-3, we demonstrate the convergence of TaSK with bond dimension D^* and number of Krylov steps \mathcal{N}_{kr} . In Sec. S-4, we compare results from TaSK with those obtained using time-dependent variational principle (TDVP) for the Heisenberg model. Sections S-5 to S-7 are devoted to our Hubbard cylinder study; they provide analytical details elucidating the origin of particle-hole asymmetry of our TaSK results for spectral quantities reported in the main text. Section S-5 discusses the computation of the second-order self-energy for the t - t_n - U model and identifies scattering processes that lead to particle-hole asymmetry. In Sec. S-6, we use the insights from Sec. S-5 to derive Eq. (12) of the main text; Sec. S-7 shows how next-nearest neighbor terms arise in the dispersion of Green's function zeros from nearest-neighbor DAH.

S-1. TASK: TECHNICAL DETAILS

Below, we detail the working procedure for TaSK: how to apply the projected Hamiltonian $H^{1\perp}$, how to prepare the initial state $|\Psi_0\rangle = \mathcal{P}^{1\perp} O_{\mathbf{k}} |\Psi_g\rangle$, and how to combine all this in the context of a Lanczos scheme.

A. Ground State Isometries

The ground-state MPS Ψ_g is the centerpiece of the TaSK method. Besides serving as an input in Eq. (6), its constituent tensors form the building blocks of the tangent space projector (3) that enables this computation.

Once Ψ_g has converged to the desired accuracy, for instance via DMRG, the first step is to bring it to left- and right-canonical forms or equivalently to determine isometries $A_\ell(\blacktriangledown)$ and $B_\ell(\blacktriangleright)$ for $\ell \in [1, \mathcal{L}]$. They satisfy

the following orthogonality relations

$$A_\ell^\dagger A_\ell = \begin{array}{c} A_\ell \\ \bigcirc \\ A_\ell^* \end{array} = \left(= \mathbb{1}_\ell^\kappa \quad B_\ell B_\ell^\dagger = \begin{array}{c} B_\ell \\ \bigcirc \\ B_\ell^* \end{array} = \right) = \mathbb{1}_{\ell-1}, \quad (\text{S1})$$

indicating that A_ℓ (B_ℓ) is a left (right) isometry, mapping a larger *parent* (\mathbb{P}) space of dimension $D_{\ell-1}d$ to a smaller D_ℓ -dimensional *kept* (\mathbb{K}) space (the definition is analogous for right isometries, with the roles of the legs reversed). For consistency, these tensors are computed once and stored in the memory to avoid possible issues arising due to the ambiguity of unitary transformations in the kept space. A more detailed discussion on these isometries can be found in Ref. 24.

The orthonormality and completeness relations of the left and right isometries and their orthogonal complements, $\bar{A}_\ell(\blacktriangledown)$ and $\bar{B}_\ell(\blacktriangleright)$,

$$\begin{array}{c} \bar{A}_\ell \\ \bigcirc \\ \bar{A}_\ell^* \end{array} = \left(= \mathbb{1}_\ell^\mathbb{P}, \quad \begin{array}{c} \bar{A}_\ell \\ \bigcirc \\ \bar{A}_\ell^* \end{array} = 0, \quad \begin{array}{c} \bar{B}_\ell \\ \bigcirc \\ \bar{B}_\ell^* \end{array} = \right) = \mathbb{1}_{\ell-1}^\mathbb{D}, \quad \begin{array}{c} \bar{B}_\ell \\ \bigcirc \\ \bar{B}_\ell^* \end{array} = 0 \quad (\text{S2a})$$

$$\begin{array}{c} \blacktriangledown \\ \bigcirc \\ \blacktriangledown \end{array} + \begin{array}{c} \blacktriangledown \\ \bigcirc \\ \blacktriangledown \end{array} = \begin{array}{c} \blacktriangleright \\ \bigcirc \\ \blacktriangleright \end{array} = \mathbb{1}_\ell^\mathbb{P}, \quad \begin{array}{c} \blacktriangleright \\ \bigcirc \\ \blacktriangleright \end{array} + \begin{array}{c} \blacktriangleright \\ \bigcirc \\ \blacktriangleright \end{array} = \begin{array}{c} \blacktriangleleft \\ \bigcirc \\ \blacktriangleleft \end{array} = \mathbb{1}_{\ell-1}^\mathbb{D}, \quad (\text{S2b})$$

form the backbone of most subsequent derivations. We note that in this work, we never explicitly determine the orthogonal complements. To reduce the computational cost, any projection to the *discarded* (\mathbb{D}) space, involving tensors $\bar{A}_\ell(\blacktriangledown)$ and $\bar{B}_\ell(\blacktriangleright)$, is performed implicitly via Eq. (S2b). Furthermore, in the following sections, any white tensor \blacktriangleright is associated with the local kept space of the left isometry A_ℓ at $\ell \in [1, \mathcal{L}]$. Similarly, gray shaded tensors \blacktriangledown have been projected to the local discarded space of \bar{A}_ℓ .

As emphasized in the main text, we limit our numerical computations to $\mathbb{V}^{1\perp} = \mathbb{V}^{1s} / \text{span}(|\Psi_g\rangle)$, where wavefunctions have the form

$$\Psi^{1\perp} = \sum_{\ell=1}^{\mathcal{L}} \begin{array}{c} \blacktriangledown \blacktriangledown \blacktriangledown \blacktriangledown \blacktriangledown \\ \blacktriangleright \blacktriangleright \blacktriangleright \blacktriangleright \blacktriangleright \\ \blacktriangledown \blacktriangledown \blacktriangledown \blacktriangledown \blacktriangledown \end{array} \begin{array}{c} T^\ell \\ \bigcirc \\ A_\ell^* \end{array}, \quad \text{with} \quad \begin{array}{c} T^\ell \\ \bigcirc \\ A_\ell^* \end{array} = 0. \quad (\text{S3})$$

The gauge choice guarantees that all terms in the sum are mutually orthogonal and can be written as

$$\begin{array}{c} T^\ell \\ \bigcirc \\ \blacktriangleright \end{array} = \begin{array}{c} \blacktriangledown \blacktriangleright \blacktriangledown \\ \bigcirc \\ \blacktriangleright \end{array}. \quad (\text{S4})$$

The presence of \blacktriangledown makes it explicit that $|\Psi^{1\perp}\rangle \in \mathbb{V}^{1\perp}$

is orthogonal to $|\Psi_g\rangle$. In that way, we directly target excitations, and our Lanczos scheme avoids recomputing $|\Psi_g\rangle$ in cases when operator $O_{\mathbf{k}}$ in Eq. (6) has a non-zero ground-state expectation value.

B. Application of the Hamiltonian

The main step of the Lanczos scheme is applying the projected Hamiltonian $H^{1\perp} = \mathcal{P}^{1\perp} H \mathcal{P}^{1\perp}$ to a state $|\Psi_i\rangle \in \mathbb{V}^{1\perp}$. Assuming that $|\Psi_i\rangle$ is described by tensors $T_i^{\ell'}$, one wants to compute tensors T_{i+1}^ℓ which describe the vector $|\Psi_{i+1}\rangle = H^{1\perp}|\Psi_i\rangle$. For a given site ℓ , this amounts to evaluating a sum of the following diagrams:

$$T_{i+1}^\ell \leftarrow \sum_{\ell'=1}^{\mathcal{L}} \left(\text{Diagram with } T_i^{\ell'} \text{ and } L_{\ell-1} \text{ and } R_{\ell+1} \text{ tensors} \right), \quad (\text{S5})$$

and projecting it to the discarded space using appropriate isometries

$$T_{i+1}^\ell \leftarrow T_{i+1}^\ell - \left(\text{Diagram with } T_{i+1}^* \text{ and } A_\ell \text{ tensors} \right). \quad (\text{S6})$$

As noted earlier, the latter is diagrammatically indicated by depicting the resulting tensors as gray. In the formulas above, the first projection with respect to $\mathcal{P}^{1\perp}$ in the definition of $H^{1\perp}$ is implicit since $|\Psi_i\rangle \in \mathbb{V}^{1\perp}$.

The sum in Eq. (S5) can be subdivided into three terms

$$\begin{aligned} T_{i+1}^\ell \leftarrow & \sum_{\ell'=1}^{\ell-1} \left(\text{Diagram with } T_i^{\ell'} \text{ and } L_{\ell-1} \text{ and } R_{\ell+1} \text{ tensors} \right) + \left(\text{Diagram with } T_i^{\ell'} \text{ and } L_{\ell-1} \text{ and } R_{\ell+1} \text{ tensors} \right) \\ & + \sum_{\ell'=\ell+1}^{\mathcal{L}} \left(\text{Diagram with } T_i^{\ell'} \text{ and } L_{\ell-1} \text{ and } R_{\ell+1} \text{ tensors} \right), \quad (\text{S7}) \end{aligned}$$

where L_ℓ and R_ℓ indicate intermediate left and right environments defined as

$$L_\ell = \left\{ \begin{array}{c} \text{Diagram with } T_i^{\ell'} \text{ and } L_{\ell-1} \text{ and } R_{\ell+1} \text{ tensors} \\ \text{Diagram with } T_i^{\ell'} \text{ and } L_{\ell-1} \text{ and } R_{\ell+1} \text{ tensors} \end{array} \right\}, \quad (\text{S8a})$$

$$R_\ell = \left\} \begin{array}{c} \text{Diagram with } T_i^{\ell'} \text{ and } L_{\ell-1} \text{ and } R_{\ell+1} \text{ tensors} \\ \text{Diagram with } T_i^{\ell'} \text{ and } L_{\ell-1} \text{ and } R_{\ell+1} \text{ tensors} \end{array} \right\}. \quad (\text{S8b})$$

They can be computed recursively by introducing the appropriate $A_{\bar{\ell}}(\nabla)$ and $B_{\bar{\ell}}(\nabla)$ tensors, starting from $L_0 = 1$, $R_{\mathcal{L}+1} = 1$.

In addition, to evaluate the terms corresponding to $\ell' < \ell$ and $\ell' > \ell$, we introduce a second type of environment,

\mathcal{L}_ℓ and \mathcal{R}_ℓ , containing $T_i^{\ell'}$ tensors of the initial state $|\Psi_i\rangle$

$$\mathcal{L}_\ell = \left\{ \begin{array}{c} \text{Diagram with } T_i^{\ell'} \text{ and } L_{\ell-1} \text{ and } R_{\ell+1} \text{ tensors} \\ \text{Diagram with } T_i^{\ell'} \text{ and } L_{\ell-1} \text{ and } R_{\ell+1} \text{ tensors} \end{array} \right\} = \left(\text{Diagram with } T_i^{\ell'} \text{ and } L_{\ell-1} \text{ and } R_{\ell+1} \text{ tensors} \right) + \left(\text{Diagram with } T_i^{\ell'} \text{ and } L_{\ell-1} \text{ and } R_{\ell+1} \text{ tensors} \right), \quad (\text{S9a})$$

$$\mathcal{R}_\ell = \left\} \begin{array}{c} \text{Diagram with } T_i^{\ell'} \text{ and } L_{\ell-1} \text{ and } R_{\ell+1} \text{ tensors} \\ \text{Diagram with } T_i^{\ell'} \text{ and } L_{\ell-1} \text{ and } R_{\ell+1} \text{ tensors} \end{array} \right\} = \left(\text{Diagram with } T_i^{\ell'} \text{ and } L_{\ell-1} \text{ and } R_{\ell+1} \text{ tensors} \right) + \left(\text{Diagram with } T_i^{\ell'} \text{ and } L_{\ell-1} \text{ and } R_{\ell+1} \text{ tensors} \right) \quad (\text{S9b})$$

This allows us to rewrite Eq. (S7) in a compact form

$$T_{i+1}^\ell \leftarrow \left(\text{Diagram with } T_i^{\ell'} \text{ and } L_{\ell-1} \text{ and } R_{\ell+1} \text{ tensors} \right) + \left(\text{Diagram with } T_i^{\ell'} \text{ and } L_{\ell-1} \text{ and } R_{\ell+1} \text{ tensors} \right) + \left(\text{Diagram with } T_i^{\ell'} \text{ and } L_{\ell-1} \text{ and } R_{\ell+1} \text{ tensors} \right), \quad (\text{S10})$$

which represents how T_{i+1}^ℓ is computed numerically.

The scheme presented above can be readily generalized to construct higher-degree excitations that live beyond $\mathbb{V}^{1\perp}$ (see Sec. V of Ref. 24 on n -site excitation Ansatz). In practice, the computational cost of such a construction scales as $\mathcal{O}(D^3 d^m w)$. In this work, we restrict our attention to the computationally cheapest case of $n = 1$.

C. Initialization

To construct the initial state $|\Psi_0\rangle = \mathcal{P}^{1\perp} O_{\mathbf{k}} |\Psi_g\rangle$, we apply $O_{\mathbf{k}} = \sum_{\ell=1}^{\mathcal{L}} O_\ell$, a linear combination of local operators, to $|\Psi_g\rangle$ in the left-canonical form,

$$|\Psi_0\rangle = \sum_{\ell=1}^{\mathcal{L}} \sum_{\ell'=1}^{\mathcal{L}} \left(\text{Diagram with } O_\ell \text{ and } L_{\ell-1} \text{ and } R_{\ell+1} \text{ tensors} \right) \quad (\text{S11a})$$

$$= \sum_{\ell'=1}^{\mathcal{L}} \left(\text{Diagram with } T_0^{\ell'} \text{ and } L_{\ell-1} \text{ and } R_{\ell+1} \text{ tensors} \right). \quad (\text{S11b})$$

Using the orthogonality relations (S2), we can determine $T_0^{\ell'}$ through the expression

$$T_0^{\ell'} \leftarrow \sum_{\ell=1}^{\mathcal{L}} \left(\text{Diagram with } O_\ell \text{ and } L_{\ell-1} \text{ and } R_{\ell+1} \text{ tensors} \right), \quad (\text{S12})$$

which can be computed using intermediate environments by analogy to Section S-1 B, and then project to the discarded space as in Eq. (S6).

Since $O_{\mathbf{k}}$ is a sum of local operators, the initial-state projection is exact, in the sense that $O_{\mathbf{k}} |\Psi_g\rangle = |\Psi_0\rangle + \langle O_{\mathbf{k}} | \Psi_g \rangle$.

D. Lanczos Scheme

In this section, we present details on the Lanczos scheme implementation within TaSK. We start with a compact summary in equation format and then elucidate each step through corresponding tensor-network diagrams.

The Lanczos scheme involves the following steps, repeated iteratively, starting from $i = 0$:

- (i) $|\Psi_{i+1}\rangle \leftarrow H^{1\perp}|\Psi_i\rangle$ apply $H^{1\perp}$,
- (ii) $c_j \leftarrow \langle \Psi_j | \Psi_{i+1} \rangle$, $j \leq i$ compute overlaps,
- (iii) Set $a_i = c_i$,
- (iv) $|\Psi_{i+1}\rangle \leftarrow |\Psi_{i+1}\rangle - \sum_j c_j |\Psi_j\rangle$, orthogonalize,
- (v) Fix gauge to match (S4),
- (vi) $b_{j+1}^2 = \langle \Psi_{i+1} | \Psi_{i+1} \rangle$ compute norm,
 $|\Psi_{i+1}\rangle \leftarrow |\Psi_{i+1}\rangle / b_{i+1}$ normalize,
- (vii) Repeat steps (ii) and (iv)-(vi) once.

(S13)

The reason for repeating steps as specified in (vii) is to reduce the round-off error noise, thereby improving numerical stability. For the same reason, the orthogonalization of $|\Psi_{i+1}\rangle$ w.r.t. to $|\Psi_j\rangle$ in step (iv) is performed for all $0 \leq j \leq i$. (With exact arithmetic, it would suffice to do this only for $j = i$ and $j = i - 1$.)

In the Krylov basis $\{|\Psi_0\rangle, \dots, |\Psi_{N_{\text{kr}}}\rangle\}$ obtained after N_{kr} iterations the matrix $H^{1\perp}$ is tridiagonal,

$$H^{1\perp} = \begin{pmatrix} a_0 & b_1 & 0 & \cdots & 0 & 0 \\ b_1 & a_1 & b_2 & \cdots & 0 & 0 \\ 0 & b_2 & a_2 & \cdots & 0 & 0 \\ \vdots & \vdots & \vdots & \ddots & \vdots & \vdots \\ 0 & 0 & 0 & \cdots & a_{N_{\text{kr}}-1} & b_{N_{\text{kr}}} \\ 0 & 0 & 0 & \cdots & b_{N_{\text{kr}}} & a_{N_{\text{kr}}} \end{pmatrix}. \quad (\text{S14})$$

Diagonalizing it yields a set of real discrete frequencies and corresponding spectral weights, $\{\omega_\alpha, S_\alpha\}$.

We now elaborate on Lanczos steps (i)-(vi) in diagrammatic format. The Hamiltonian $H^{1\perp}$ is applied to $|\Psi_i\rangle$ according to the procedure described in Section S-1 B:

$$\begin{array}{c} T_i^{\ell'} \\ \vdots \end{array} \xrightarrow{H^{1\perp}} \begin{array}{c} T_{i+1}^\ell \\ \vdots \end{array}. \quad (\text{S15})$$

Next, the overlaps $c_j = \langle \Psi_j | \Psi_{i+1} \rangle$, $j \leq i$ are computed,

$$c_j = \sum_\ell \begin{array}{c} T_{i+1}^\ell \\ \vdots \\ T_j^\ell \end{array}, \quad (\text{S16})$$

and used to orthogonalize the new Krylov vector, $|\Psi_{i+1}\rangle$ w.r.t. previous Krylov vectors,

$$\begin{array}{c} T_{i+1}^\ell \\ \vdots \end{array} \leftarrow \begin{array}{c} T_{i+1}^\ell \\ \vdots \end{array} - \sum_j c_j \begin{array}{c} T_j^\ell \\ \vdots \end{array}, \quad (\text{S17})$$

Then, $|\Psi_{i+1}\rangle$ is projected to the discarded space to ensure the desired gauge (S4) of its constituent tensors

$$\begin{array}{c} T_{i+1}^\ell \\ \vdots \end{array} \leftarrow \begin{array}{c} T_{i+1}^\ell \\ \vdots \end{array} - \begin{array}{c} T_{i+1}^\ell \\ \vdots \\ A_\ell^* \\ \vdots \\ A_\ell \end{array}. \quad (\text{S18})$$

This step prevents numerical noise from spoiling the gauge condition from Eq. (S4) and would not be needed with

exact arithmetic. Finally, the new Krylov vector is normalized,

$$\begin{array}{c} T_{i+1}^\ell \\ \vdots \end{array} \leftarrow \begin{array}{c} T_{i+1}^\ell \\ \vdots \end{array} \cdot b_{i+1}^{-1} \quad b_{i+1}^2 := \sum_\ell \begin{array}{c} T_{i+1}^\ell \\ \vdots \\ T_{i+1}^\ell \end{array}. \quad (\text{S19})$$

Here, b_{i+1} corresponds to the superdiagonal element of $H^{1\perp}$ in the Krylov basis.

As mentioned above in step (vii) of Eq. (S13), we find that performing the orthonormalization steps (S17), (S18), and (S19) a second time improves numerical stability by reducing roundoff-error noise. This does not introduce significant overhead, since orthonormalization scales as $\mathcal{O}(\mathcal{L}D^2d)$ and is therefore much cheaper than the application of the Hamiltonian ($\mathcal{O}(\mathcal{L}D^3wd)$).

E. Error Measure

In the main text, we proposed an error measure $\delta_\alpha = (\Delta_\alpha^{2\perp})^{1/2}$ based on the 2-site variance, $\Delta_\alpha^{2\perp} = \|\mathcal{P}^{2\perp} H |\Psi_\alpha^{1\perp}\rangle\|^2$ [cf. Eq. (9)], where $|\Psi_\alpha^{1\perp}\rangle$ is an eigenstate of the Krylov Hamiltonian. To compute the latter, we have to apply H to a tangent vector, followed by a projection to $\mathbb{V}^{2\perp}$ using the projector

$$\mathcal{P}^{2\perp} = \begin{array}{c} \text{---} \\ \text{---} \\ \text{---} \\ \text{---} \\ \text{---} \\ \text{---} \end{array} \begin{array}{c} \text{---} \\ \text{---} \\ \text{---} \\ \text{---} \\ \text{---} \\ \text{---} \end{array}. \quad (\text{S20})$$

This can be achieved with a small modification of the algorithm to apply $H^{1\perp}$, described in Sec. S-1 B.

Consider for now a generic state $|\Psi^{1\perp}\rangle \in \mathbb{V}^{1\perp}$, described by the tensors $T^{\ell'}$ with gauge constraint as in Eq. (S4). Reusing the environments defined in Sec. S-1 B, we obtain

$$\begin{array}{c} T_{2s}^{\ell'} \\ \vdots \end{array} \leftarrow \sum_{\ell'=1}^{\mathcal{L}} \begin{array}{c} T^{\ell'} \\ \vdots \\ \text{---} \\ \text{---} \\ \text{---} \\ \text{---} \end{array} \quad (\text{S21})$$

$$= \begin{array}{c} \text{---} \\ \text{---} \\ \text{---} \\ \text{---} \end{array} + \begin{array}{c} \text{---} \\ \text{---} \\ \text{---} \\ \text{---} \end{array} + \begin{array}{c} \text{---} \\ \text{---} \\ \text{---} \\ \text{---} \end{array} + \begin{array}{c} \text{---} \\ \text{---} \\ \text{---} \\ \text{---} \end{array}.$$

By projecting $T_{2s}^{\ell'}$ to the discarded spaces with \bar{A}_ℓ and $\bar{B}_{\ell+1}$ using Eq. (S2), we get

$$\begin{array}{c} T_{2s}^{\ell'} \\ \vdots \end{array} \leftarrow \sum_{\ell'=1}^{\mathcal{L}} \begin{array}{c} T^{\ell'} \\ \vdots \\ \bar{A}_\ell \\ \vdots \\ \bar{B}_{\ell+1} \end{array}. \quad (\text{S22})$$

With that, we finally obtain its 2-site variance,

$$\Delta^{2\perp} = \|\mathcal{P}^{2\perp} H |\Psi^{1\perp}\rangle\|^2 = \sum_\ell \|T_{2\perp}^\ell\|^2. \quad (\text{S23})$$

We note that the best practice is to compute $\Delta_\alpha^{2\perp}$ for chosen eigenstates $|\Psi_\alpha^{1\perp}\rangle$ of the Krylov Hamiltonian,

specifically those corresponding to the most prominent spectral weights. If $\Delta_{\alpha}^{2\perp}$ is required for *all* eigenstates, we can instead compute $T_{2\perp}^{\ell}$ for each Krylov basis vector $|\Psi_i\rangle$ on the fly, while applying $H^{1\perp}$ inside the Lanczos loop (S13). This allows us to directly reuse the environments computed during the Hamiltonian-application step (see Sec. S-1 B) to also compute T_{2s}^{ℓ} via Eq. (S21), followed by the projection Eq. (S22). Then, after terminating the Krylov scheme and determining the eigenbasis of the Krylov Hamiltonian, we subject the collected $T_{2\perp}^{\ell}$ to the transformation to the Krylov eigenbasis before evaluating Eq. (S23).

S-2. BROADENING OF DISCRETE SPECTRA

The spectra obtained through TaSK are discrete. In this section, we describe the broadening strategy we employ to obtain continuous spectral functions. Our broadening scheme can be used for generic discrete spectral functions with $N + 1$ spectral peaks. Within TaSK, we have $N = \mathcal{N}_{\text{kr}}$ (or $\mathcal{N}_{\text{kr}} + 1$ for non-zero $\langle O_{\mathbf{k}} \rangle$ in Eq. (8) of the main text). In the following,

$$A^{\text{d}}(\omega) = \sum_{\alpha=0}^N A_{\alpha} \delta(\omega - \omega_{\alpha}) \quad (\text{S24})$$

refers to a discrete spectral function with (real, positive) spectral weights A_{α} and discrete frequencies ω_{α} . The continuous, broadened spectral function is referred to as $A^{\text{b}}(\omega)$. If an expression does not specify a superscript d or b, it holds for both discrete and broadened data. Superscripts are also specified for quantities derived from the spectra, such as the Green's function

$$G(z) = \int_{-\infty}^{\infty} d\omega \frac{A(\omega)}{z - \omega}, \quad z \in \mathbb{C}, \quad (\text{S25})$$

or its retarded version, $G^R(\omega) = G(\omega + i0^+)$.

A. Gaussian broadening

To broaden the discrete spectra, we use a Gaussian kernel,

$$g_{\sigma}(\omega, \omega') = \frac{1}{\sqrt{2\pi}\sigma} \exp\left(-\frac{(\omega - \omega')^2}{2\sigma^2}\right), \quad (\text{S26})$$

and obtain the broadened, continuous spectrum as

$$\begin{aligned} A^{\text{b}}(\omega) &= \int_{-\infty}^{\infty} d\omega' g_{\sigma}(\omega, \omega') A^{\text{d}}(\omega') \\ &= \sum_{\alpha=0}^N g_{\sigma}(\omega, \omega_{\alpha}) A_{\alpha}. \end{aligned} \quad (\text{S27})$$

The corresponding real part can be computed via Kramers-Kronig relations.

Let μ_n denote the n -th moment of the spectral function:

$$\mu_n = \int_{-\infty}^{\infty} d\omega \omega^n A(\omega). \quad (\text{S28})$$

Gaussian broadening preserves the weight, $\mu_0^{\text{b}} = \mu_0^{\text{d}}$, and first moment, $\mu_1^{\text{b}} = \mu_1^{\text{d}}$, of the discrete spectral function $A^{\text{d}}(\omega)$, but not the higher moments, e.g. $\mu_2^{\text{b}} = \mu_2^{\text{d}} + \sigma^2 \mu_0^{\text{d}}$. It is of course unavoidable (and intended) that high-order moments of the discrete and broadened data eventually differ. However, it is desirable for the broadening scheme to conserve some low-order moments beyond μ_0 and μ_1 , since low-order moments control the short-time dynamics of the retarded Green's function, $G^R(t) = \int_{-\infty}^{\infty} \frac{d\omega}{2\pi} G^R(\omega) e^{-i\omega t}$.

$$\mu_n = -\text{Im} \left[(i\partial_t)^n G^R(t) \right]_{t=0^+} \quad (\text{S29a})$$

$$G^R(t) = -i\theta(t) \int_{-\infty}^{\infty} d\omega A(\omega) e^{-i\omega t}. \quad (\text{S29b})$$

This short-time dynamics is controlled by physics on short distances, for which finite-size effects or MPS truncation errors should be small. A broadening strategy that preserves low-order moments is described in the next section. It is based on representing the discrete Green's function $G^{\text{d}}(z)$ through a continued fraction expansion (CFE) of finite depth, then using the tail-end part of the expansion to define a discrete residual function, and finally applying Gaussian broadening to the latter.

B. Continued fraction expansion

It is a well-known fact [18] that any Green function of the form (S25) can be represented via a CFE of the form

$$G(z) = \frac{t_0^2}{z - \epsilon_0 - \frac{t_1^2}{z - \epsilon_1 - \dots}}. \quad (\text{S30})$$

If the spectral function $A(\omega)$ of $G(z)$ is known, the corresponding CFE coefficients can be obtained using a Lanczos scheme. Here, we describe this scheme for the case, relevant for this paper, of a discrete spectral function $A^{\text{d}}(\omega)$ of the form (S24), with $\alpha = 0, \dots, N$. Then, the discrete Green's function can be expressed as

$$G^{\text{d}}(z) = \sum_{\alpha=0}^N \frac{A_{\alpha}}{z - \omega_{\alpha}} \quad (\text{S31a})$$

$$= t_0^2 \sum_{\alpha=0}^N \langle v_0 | e_{\alpha} \rangle [(z - \Omega)^{-1}]_{\alpha\alpha} \langle e_{\alpha} | v_0 \rangle, \quad (\text{S31b})$$

where Ω is a diagonal matrix with elements $\Omega_{\alpha\alpha'} = \langle e_{\alpha} | \Omega | e_{\alpha'} \rangle = \delta_{\alpha\alpha'} \omega_{\alpha}$, and the normalized vector $|v_0\rangle$ has components $\langle e_{\alpha} | v_0 \rangle = \sqrt{A_{\alpha}}/t_0$, with $t_0^2 = \sum_{\alpha} A_{\alpha}$. Since $G^{\text{d}}(z)$ has $N + 1$ poles, the corresponding CFE (S30) will terminate at depth $N + 1$. Given the weights and frequencies $\{A_{\alpha}, \omega_{\alpha}\}$, the CFE coefficients for $G^{\text{d}}(z)$ can be computed as follows: Use the Lanczos algorithm,

initialized with $|v_0\rangle$, to construct a set of orthonormal Krylov vectors $\{|v_0\rangle, |v_1\rangle, \dots, |v_N\rangle\}$ that span the Krylov space $K_N = \text{span}\{|v_0\rangle, \Omega|v_0\rangle, \dots, \Omega^N|v_0\rangle\}$. When Ω is expressed in the Krylov basis it takes the form of a matrix M , with elements $M_{nn'} = \sum_\alpha \langle v_n | e_\alpha \rangle \omega_s \langle e_\alpha | v_{n'} \rangle$, that has a tridiagonal form:

$$M = \begin{pmatrix} \epsilon_0 & t_1 & 0 & \cdots & 0 & 0 \\ t_1 & \epsilon_1 & t_2 & \cdots & 0 & 0 \\ 0 & t_2 & \epsilon_2 & \cdots & 0 & 0 \\ \vdots & \vdots & \vdots & \ddots & \vdots & \vdots \\ 0 & 0 & \cdots & \epsilon_{N-2} & t_{N-1} & 0 \\ 0 & 0 & \cdots & t_{N-1}^\dagger & \epsilon_{N-1} & t_N \\ 0 & 0 & \cdots & 0 & t_N & \epsilon_N \end{pmatrix}. \quad (\text{S32})$$

Using a standard formula for the inverse of a block matrix, the Green's function (S31b) can thus be expressed through the top-left element of the matrix $(z - M)^{-1}$, as

$$G^d(z) = t_0^2 [(z - M)^{-1}]_{00}. \quad (\text{S33})$$

Equation (S33) immediately implies a depth- $(N+1)$ CFE of the form (S30), with CFE coefficients $\{\epsilon_n, t_n\}$ given by the diagonal and next-to-diagonal elements of M , and terminated by $-t_N^2/(z - \epsilon_N)$, see for instance Eqs. (23-25) of Ref. 18. This CFE gives an exact representation of $G^d(z)$ and hence still represents a discrete Green's function. A scheme for broadening it is described next.

The CFE coefficients are related to the moments $\mu_n = \langle v_0 | \Omega^n | v_0 \rangle$. In particular, if the CFE coefficients up to depth $m+1$ (i.e. ϵ_0, t_0 to ϵ_m, t_m) of two Green's functions are identical, their first $2m+2$ moments, $\mu_0, \dots, \mu_{2m+1} = \langle v_0 | \Omega^m \cdot \Omega \cdot \Omega^m | v_0 \rangle$, are also identical. The reason is the matrix representations of the Ω s of both Green's functions coincide within their respective depth $m+1$ Krylov spaces $K_m = \text{span}(|v_0\rangle, \Omega|v_0\rangle, \dots, \Omega^m|v_0\rangle)$.

C. Broadening the residual function

We seek a scheme for broadening $G^d(z)$ that preserves the first $2m+2$ moments, with m typically much smaller than N . To achieve this, the low-order CFE coefficients with $n \leq m$ of the broadened Green's function $G^b(z)$ should coincide with those of the discrete $G^d(z)$. We therefore express the latter as

$$G^d(z) = \frac{t_0^2}{z - \epsilon_0 - \frac{t_1^2}{z - \epsilon_1 - \cdots - \frac{t_m^2}{z - \epsilon_m - R_m^d(z)}}}, \quad (\text{S34})$$

where we have used the CFE coefficients with $n > m$ to define the residual function

$$R_m^d(z) = \frac{t_{m+1}^2}{z - \epsilon_{m+1} - \frac{t_{m+2}^2}{z - \epsilon_{m+2} - \cdots - \frac{t_N^2}{z - \epsilon_N}}}. \quad (\text{S35})$$

This function, being defined through a finite-depth CFE, itself represents a discrete Green's function. The key idea is now to broaden this residual function (using the Gaussian kernel of Sec. S-2 A) to obtain a continuous version, $R_m^b(z)$. Inserting the latter into the CFE (S34) then yields the desired continuous, broadened Green's function

$$G^c(z) = \frac{t_0^2}{z - \epsilon_0 - \frac{t_1^2}{z - \epsilon_1 - \cdots - \frac{t_m^2}{z - \epsilon_m - R_m^b(z)}}}. \quad (\text{S36})$$

Since $G^c(z)$ and $G^d(z)$ have the same CFE coefficients for $n \leq m$, their first $2m+2$ moments are equal, too.

The CFE form (S35) of $R^d(z)$ is not convenient for computing its convolution with a Gaussian kernel. Instead, we first express it in the form of a spectral representation analogous to Eq. (S31b). To this end, we reverse the steps leading from Eq. (S31b) to (S33). We express $R_m^d(z)$ as

$$R_m^d(z) = t_{m+1}^2 [(z - \widetilde{M})^{-1}]_{00}, \quad (\text{S37})$$

involving the top-left element of the matrix $(z - \widetilde{M})^{-1}$, where \widetilde{M} is the matrix

$$\widetilde{M} = \begin{pmatrix} \epsilon_{m+1} & t_{m+2} & 0 & \cdots & 0 & 0 \\ t_{m+2} & \epsilon_{m+2} & t_{m+3} & \cdots & 0 & 0 \\ 0 & t_{m+3} & \epsilon_{m+3} & \cdots & 0 & 0 \\ \vdots & \vdots & \vdots & \ddots & \vdots & \vdots \\ 0 & 0 & \cdots & \epsilon_{N-2} & t_{N-1} & 0 \\ 0 & 0 & \cdots & t_{N-1}^\dagger & \epsilon_{N-1} & t_N \\ 0 & 0 & \cdots & 0 & t_N & \epsilon_N \end{pmatrix}. \quad (\text{S38})$$

In other words, \widetilde{M} is a submatrix of M , with elements $\widetilde{M}_{nn'} = \langle \widetilde{v}_n | M | \widetilde{v}_{n'} \rangle$, where we defined $|\widetilde{v}_n\rangle = |v_{m+1+n}\rangle$ for $n = 0, \dots, N - m - 1$. We diagonalize this matrix to find its eigenvalues $\widetilde{\omega}_\alpha$ and eigenvectors $|\widetilde{e}_\alpha\rangle$, so that its elements can be expressed as $\widetilde{M}_{nn'} = \sum_{\alpha=0}^{N-m-1} \langle \widetilde{v}_n | \widetilde{e}_\alpha \rangle \widetilde{\omega}_\alpha \langle \widetilde{e}_\alpha | \widetilde{v}_{n'} \rangle$. By analogy to Eq. (S31b), $R_m^d(z)$ thus has a spectral representation of the form

$$R_m^d(z) = t_{m+1}^2 \sum_{\alpha=0}^{N-m-1} \frac{|\langle \widetilde{e}_\alpha | \widetilde{v}_0 \rangle|^2}{z - \widetilde{\omega}_\alpha}, \quad (\text{S39})$$

from which we can read off the discrete weights and frequencies defining its spectral function.

Broadening the latter through convolution with a Gaussian using Eq. (S27), as discussed in Sec. S-2 A, we obtain the desired continuous, broadened residual function $R_m^b(z)$, to be inserted into Eq. (S36) for $G^b(z)$. Since Gaussian broadening conserves the zeroth and first moments of the residual function, the above scheme conserves the first $2m+3$ moments of $A(\omega)$, μ_0, \dots, μ_{2m+2} .

In subsequent sections on numerical results, we will denote the depth of the CFE up to the residual function by $\mathcal{N}_{\text{CFE}} = m + 1$.

S-3. CONVERGENCE

TaSK method is subject to two sources of error: (i) the projection error arising from the tangent-space projection of the Hamiltonian, $H \rightarrow H^{1\perp}$, and (ii) an error due to an insufficient number of Krylov steps \mathcal{N}_{kr} . Since the dimension of $\mathbb{V}^{1\perp}$ scales as $\mathcal{O}(\mathcal{L}D^2d)$, we can address the former by performing a more precise ground-state (GS) calculation with larger bond dimension D , while the latter can be reduced by simply increasing \mathcal{N}_{kr} .

To control the projection error, we fix a bond-dimension threshold for the GS and expand D during the DMRG GS search using DMRG3S-like mixing [46] together with controlled bond expansion [47] (see specifically Sec. 3 of the supplemental material of Ref. 47 and also Ref. 48) until this threshold is saturated. None of the models tested here have an exact MPS representation of the ground state. However, for the $\mathcal{L} = 64$ site Heisenberg model, our choice $D^* = 512$ is so large that the ground state energy is converged to machine precision. Note that for models like the AKLT model, where the ground state has an exact, finite bond-dimension MPS representation, the strategy of expanding the tangent space by means of a more accurate GS calculation does not work. In these cases, some tangent-space expansion method is needed, a technical development left for future work.

In the following sections, we explore TaSK's convergence with bond dimension D (or, in our case, the number of $\text{SU}(2)$ multiplets D^*) and the number of Krylov steps \mathcal{N}_{kr} . In Sec. S-3 A, we discuss how the discrete spectra of the two benchmark spin-chain models, the Haldane-Shastry and the Heisenberg model, converge with \mathcal{N}_{kr} . Section S-3 B discusses the convergence of continuous spectral functions for the Hubbard model on a cylinder with both D^* and \mathcal{N}_{kr} and shows how their resolution changes depending on the choice of broadening parameters introduced in Sec. S-2.

A. Spin Models

Figure S-1 demonstrates convergence of discrete frequencies ω_α with the number of Krylov steps \mathcal{N}_{kr} for (a) the Haldane-Shastry model (HSM) at $D^* = 700$, and $\mathcal{L} = 40$ and (b) the Heisenberg chain at $D^* = 512$ and $\mathcal{L} = 64$. As shown in Fig. S-1(a), the HSM exhibits rapid convergence across the entire spectrum, saturating around $\mathcal{N}_{\text{kr}} = 30$. In the low-frequency region, we observe three peaks that do not correspond to any physical excitations (when compared with analytical results for the full *un-projected* Hamiltonian). However, their weight $[S_\pi]_\alpha$ is negligible ($\sim \mathcal{O}(10^{-12})$) and their error estimate δ_α is at least three orders of magnitude higher than that of the remaining peaks on *the same energy scale* – an important distinction, since the error monotonically increases towards the high-frequency region, as shown in Fig. 1(b).

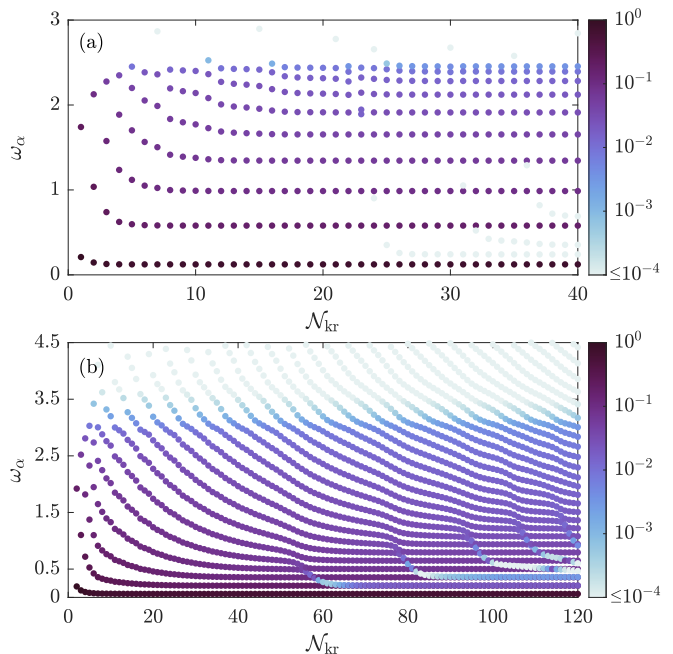


FIG. S-1. Convergence of ω_α with the number of Krylov steps \mathcal{N}_{kr} for (a) the Haldane-Shastry model on a ring of size $\mathcal{L} = 40$ with $D^* = 700$ and (b) the Heisenberg chain of length $\mathcal{L} = 64$ with $D^* = 512$. The color scale indicates spectral weights S_α , represented on a logarithmic scale. Spectral weights $\leq 10^{-4}$ are clipped to the minimum color value to highlight dominant contributions to the DSF.

We conjecture that (i) these low-weight peaks are very likely *not* ghost states as they often appear in Lanczos schemes, but (ii) rather a result of the projection to the tangent space, which modifies the Hamiltonian. The reason for conjecture (i) is that we are working with full orthonormalization (see Sec. S-1 D). As a result, the eigenstates generated by our Lanczos scheme are mutually orthogonal within machine precision (overlaps $< 10^{-16}$), i.e. they are indeed independent eigenstates of $H^{1\perp}$. Conjecture (ii), that these states result from the tangent space projection, is based on the fact that they have a large 2-site variance $\Delta_\alpha^{2\perp}$ relative to other states on the same energy scale. This means that these states have a substantial projection error, i.e. reducing the projection error, for instance by expanding \mathbb{V}^{1s} or by working with \mathbb{V}^{2s} (the space of two-contiguous-site variations w.r.t. the ground state [24]) will substantially affect these states. By contrast, the small variance of the high-weight states (see Fig. 1 of the main text and its discussion) indicates that the same reduction of the projection error hardly affects these states.

For the Heisenberg chain, the convergence of the dynamical structure factor $S_\pi(\omega)$ with \mathcal{N}_{kr} is slower than for the HSM, but systematic, as seen in Fig. S-1(b). This is expected, since the spinon excitations of the Heisenberg model are more complex and lead to dense, broadly distributed spectral weight. Nonetheless, the low-frequency part of the spectrum converges rapidly. In contrast, the

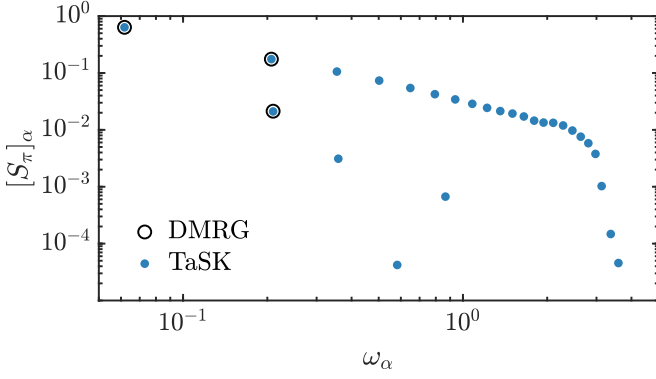


FIG. S-2. Discrete spectral data for the dynamical structure factor of the $\mathcal{L} = 64$ -site Heisenberg chain at $k = \pi$. Blue dots are computed via TaSK, black circles by targeting low-energy states with DMRG. We obtain the TaSK data in Fig. 2 by binning the data shown here, as described near the end of Sec. S-3 A.

high-frequency part is already *qualitatively* well resolved at moderate \mathcal{N}_{kr} (see Fig. 2 of the main text), whereas a *quantitative* resolution of the entire discrete spectrum would require more iterations.

For sufficiently large \mathcal{N}_{kr} , some of the low-frequency spectral peaks develop a secondary satellite that is nearly degenerate with the main peak. Even though their weight is at least about an order of magnitude lower than that of the main peak, it is nonetheless substantial, unlike in the HSM case. Since we employ full reorthogonalization, ensuring that the obtained Krylov states are mutually orthogonal within numerical accuracy, we again conclude that these indeed correspond to excitations of H^{\perp} , not Lanczos ghosts.

To check whether they are also eigenstates of the unprojected Hamiltonian H , we target the four lowest-energy triplets ($S = 1$ sector, $4 \cdot 3 = 12$ states in total) of the $\mathcal{L} = 64$ Heisenberg chain using DMRG. These are denoted $|\Psi_\alpha^s\rangle$, where $s \in \{1, 0, -1\}$ denotes the S^z eigenvalue, and are used to compute the corresponding spectral weights, $[S_\pi]_\alpha = |\langle \Psi_\alpha^0 | S_\pi^z | \Psi_g \rangle|^2$. Since one of these triplets has momentum different from π , its spectral weight is zero. Consequently, we only recover the first three spectral peaks of $S_\pi(\omega)$.

The result of this computation is shown in Fig. S-2, where we compare it with the discrete TaSK data. Evidently, the three lowest-frequency spectral peaks coincide very well, including the satellite of the second main peak. This demonstrates that at least this satellite is a genuine excitation of H , and not an artifact of the tangent space projection. Therefore, in the postprocessing of spectral data for this model, we treat all excitations of the kind as physical. Specifically, to achieve the thermodynamic-limit approximation seen in Fig. 2, the main peaks (those of larger weight) and their corresponding satellites are binned: their spectral weights are added and positioned

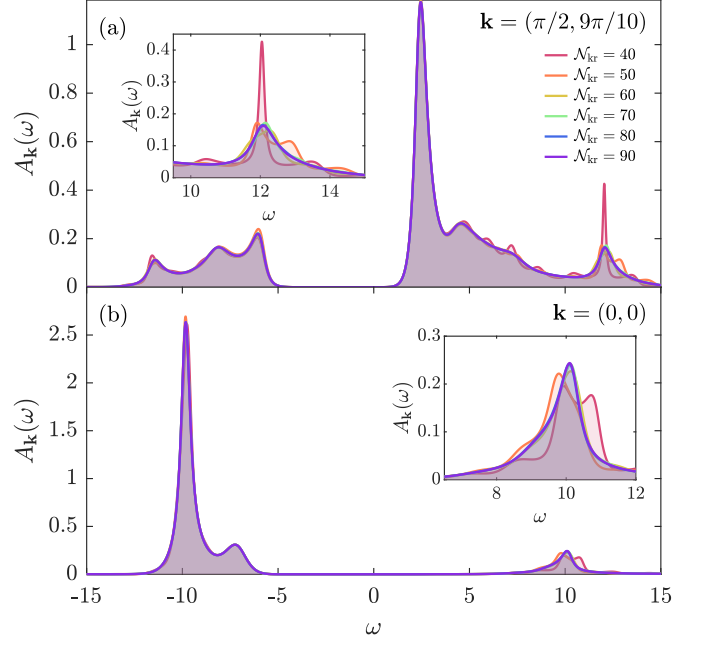


FIG. S-3. Convergence of $A_{\mathbf{k}}(\omega)$ with the number of Krylov steps \mathcal{N}_{kr} for the t - t_n - U Hubbard model with $D^* = 2000$ for (a) $\mathbf{k} = (\pi/2, 9\pi/10)$ and (b) $\mathbf{k} = \Gamma = (0, 0)$.

at

$$\tilde{\omega}_\alpha = \frac{S_{\alpha+1}\omega_{\alpha+1} + S_\alpha\omega_\alpha}{S_{\alpha+1} + S_\alpha}. \quad (\text{S40})$$

The reason for this binning is to avoid jumps in the data during the secondary binning scheme described in Sec. IV (D) of Ref. 11. There, each spectral weight S_α is rescaled by the width of the energy interval in which it resides

$$W_\alpha = \frac{\omega_{\alpha+1} - \omega_{\alpha-1}}{2}. \quad (\text{S41})$$

This is done to be able to present data points collected for different system sizes (in our case, $\mathcal{L} = 64$ and $\mathcal{L} = 128$) as a single approximation of the continuous dynamical structure factor in the thermodynamic limit. In this setup, if two contiguous frequencies ω_α and $\omega_{\alpha+1}$ are close ($< 0.1\Delta W$, where ΔW is an average spacing), the rescaling will artificially enhance or suppress a subset of spectral weights. To avoid this, instead of binning, one could, in principle, retain only the dominant excitation. However, this would compromise the total spectral weight and consequently violate the sum rule.

B. Hubbard Model

Figure S-3 demonstrates convergence of the broadened spectral function $A^{\text{b}}(\omega)$ with \mathcal{N}_{kr} for the 2D Hubbard model with density-assisted hopping. The parameters of the model (U , t , t_n) are identical to those specified in the main text. For the ground-state calculation, we retain $D^* = 2000$ SU(2) multiplets. Figures S-3(a) and S-3(b) correspond to momentum points of $\mathbf{k} = (\pi/2, 9\pi/10)$

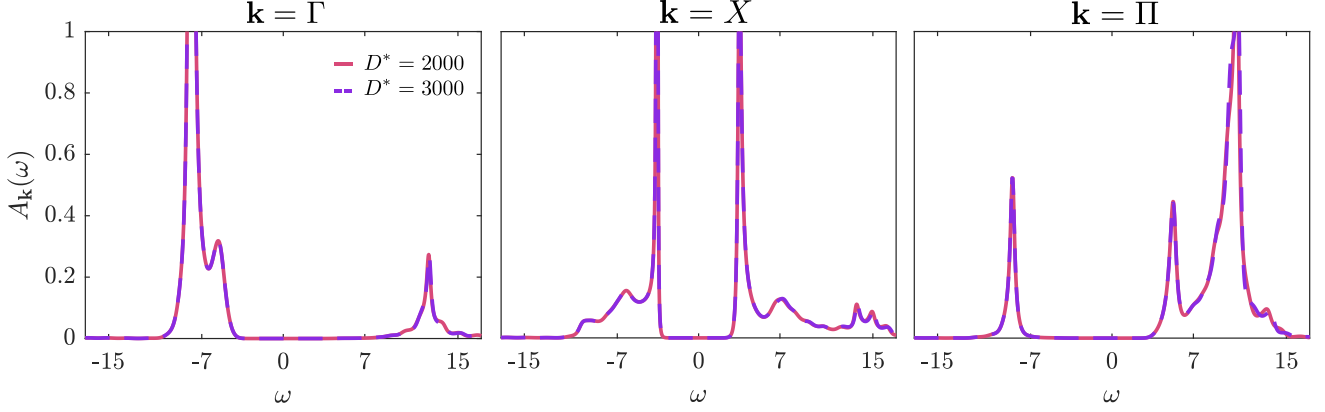


FIG. S-4. Convergence of $A_{\mathbf{k}}(\omega)$ with D^* for the t - t_n - U Hubbard model at the high symmetry points Γ , X and Π .

and $\mathbf{k} = \Gamma = (0,0)$, respectively. For the Gaussian broadening of the residual function we set the broadening parameters (defined in Sec. S-2 C) to $\sigma = 0.5$ and $\mathcal{N}_{\text{CFE}} = 2$, preserving the first 6 moments of $A_{\mathbf{k}}(\omega)$. We use $\mathcal{N}_{\text{kr}} = 50$ for the t - U and t_{eff} - U - $\delta\Sigma$ computations in the main text [Figs. 3(a,b,e,f)], and $\mathcal{N}_{\text{kr}} = 60$ for t - t_n - U [Figs. 3(c,d)], which we find sufficient for a qualitative description of the dominant spectral features.

Figure S-4 demonstrates convergence of the t - t_n - U Hubbard model with the number of $\text{SU}(2)$ multiplets D^* for $\mathbf{k} = \Gamma$, X and Π . We use $\mathcal{N}_{\text{kr}} = 50$ and set the broadening parameters as above. For the computations in the main text, we used $D^* = 3000$ (discarded weight $\xi \sim \mathcal{O}(10^{-8})$) for the pure t - U Hubbard model and (having realized that a smaller D^* would have sufficed) proceeded with $D^* = 2000$ ($\xi \sim \mathcal{O}(10^{-8})$) for t - t_n - U . As seen in Fig. S-4, spectral line cuts computed for $D^* = 2000$ and 3000 indeed coincide for the chosen values of the broadening parameters. Moreover, we find that even for $D^* = 1000$ we already recover the overall shape of the spectral function with plausible accuracy.

Finally, in Fig. S-5 we show how different choices of broadening parameters, \mathcal{N}_{CFE} and σ , influence the resolution of the broadened spectral function $A^b(\omega)$ for the t - t_n - U Hubbard model. It is to be expected that setting \mathcal{N}_{CFE} too high or similarly setting σ too low results in an underbroadened $A^b(\omega)$. As an example, we compare $A^b(\omega)$ at $\mathbf{k} = X$ for different choices of σ [Fig. S-5(a)] or \mathcal{N}_{CFE} [Fig. S-5(b)], while keeping the corresponding other broadening parameter fixed. From this, we conclude that choosing the Gaussian width σ too small leads to a uniformly underbroadened spectrum, i.e. wiggles appear across the entire frequency range. Increasing \mathcal{N}_{CFE} , on the other hand, has no substantial effect on the spectral continuum and mostly sharpens the main spectral peaks. Nevertheless, too large \mathcal{N}_{CFE} eventually leads to overly sharp main peaks, and a false occurrence of sharp peaks in the continuum. In the extreme case, when \mathcal{N}_{CFE} matches the number of discrete spectral peaks, no broadening occurs at all. The general rule is that σ controls the

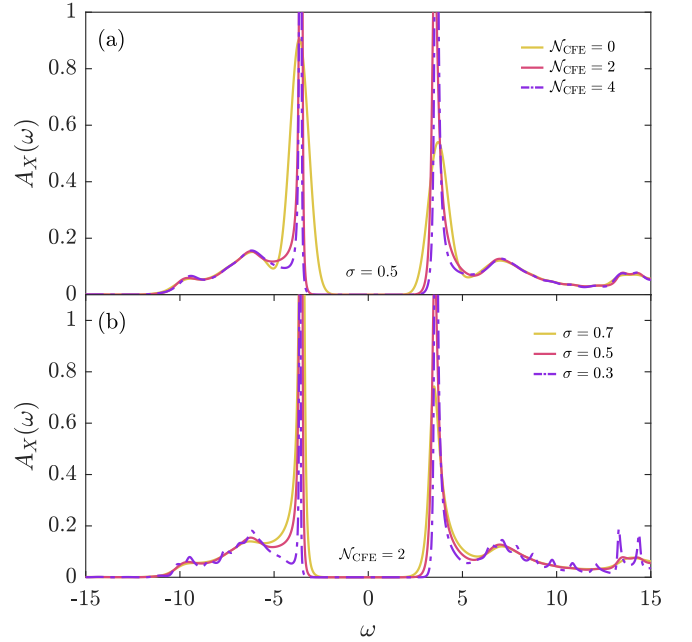


FIG. S-5. Comparison of $A_X(\omega)$ of the t - t_n - U Hubbard model for different choices of broadening parameters: (a) three values of \mathcal{N}_{CFE} at fixed $\sigma = 0.5$, and (b) three values of σ at fixed $\mathcal{N}_{\text{CFE}} = 2$.

broadening of the incoherent background and should be chosen such that wiggles are broadened out while genuine structure is not blurred. At the same time, \mathcal{N}_{CFE} controls the sharpness of the more coherent features (the “main peaks”), and should not be chosen too large to avoid the spurious occurrence of sharp peaks in the continuum. Therefore, within the scope of this work, we broaden the discrete spectral functions of the Hubbard model using $\sigma = 0.5$ and $\mathcal{N}_{\text{CFE}} = 2$, which provides a good balance between spectral resolution and smoothness.

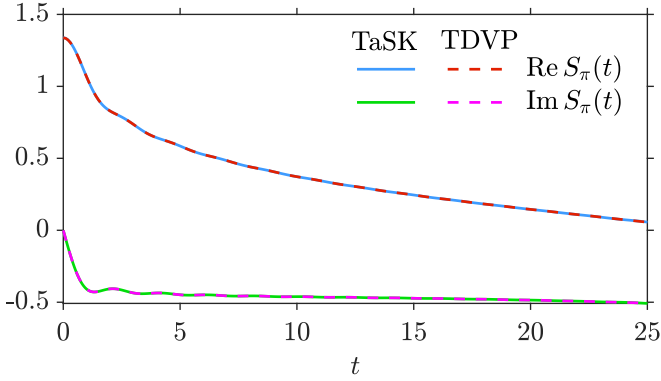


FIG. S-6. Comparison of the time-dependent correlation function of a spin- $\frac{1}{2}$ Heisenberg chain, computed via TDVP (dashed) and TaSK (solid). We use a singular value threshold of $\epsilon_{\text{svd}} = 10^{-8}$ for the TDVP, resulting in a bond dimension of at most $D^* = 502$.

S-4. COMPARISON TO TDVP

To assess the accuracy of TaSK, we compare its results with those obtained via time-dependent variational principle (TDVP) in the 64-site spin- $\frac{1}{2}$ Heisenberg chain. Specifically, we evaluate the time-dependent correlation function

$$S_\pi(t) = \langle \Psi_g | S_\pi^z e^{-i(H-E_g)t} S_\pi^z | \Psi_g \rangle, \quad (\text{S42})$$

where $S_\pi^z = \mathcal{L}^{-1/2} \sum_{\ell=1}^{\mathcal{L}} (-1)^\ell S_\ell^z$, and S_ℓ^z is the local spin- z operator on site ℓ .

We compute $S_\pi(t)$ using two different approaches. First, we time-evolve

$$|\Psi(t)\rangle = e^{-i(H-E_g)t} S_\pi^z |\Psi_g\rangle, \quad (\text{S43})$$

$$S_\pi(t) = \langle \Psi_g | S_\pi^z |\Psi(t)\rangle \quad (\text{S44})$$

using single-site TDVP with controlled bond expansion [94]. We use a third-order integrator (error of $\mathcal{O}(\delta t^4)$) and time step size $\delta t = 0.1$. We take 250 time steps, such that the largest time is 25. Truncation is done via a singular-value-decomposition threshold $\epsilon_{\text{svd}} = 10^{-8}$. The largest bond dimension encountered with this threshold is $D^* = 502$ SU(2) multiplets, similar to $D^* = 512$ in TaSK. This TDVP result serves as a benchmark.

Second, we Fourier-transform our TaSK data to the time domain,

$$S_\pi(t) = \sum_{\alpha} |\langle \Psi_{\alpha}^{\perp} | S_\pi^z | \Psi_g \rangle|^2 e^{-i\omega_{\alpha} t}, \quad (\text{S45})$$

where $(\omega_{\alpha}, |\Psi_{\alpha}^{\perp}\rangle)$ are eigenpairs of the Krylov Hamiltonian H^{\perp} , computed via TaSK.

Figure S-6 shows a comparison of the time-dependent data obtained via TaSK (solid lines) and TDVP (dashed lines), respectively. The data matches perfectly, and the deviation (not visible in the figure) is within the expected Trotter error of TDVP. This handshake between TaSK and TDVP, whose comfort zones are low energies or short times, respectively, is very satisfying: it shows that TaSK not only captures the low-energy features of the spectrum

accurately, but also describes well the high-energy features governing the short-time dynamics.

S-5. SECOND-ORDER SELF-ENERGY FOR THE HUBBARD MODEL WITH DENSITY-ASSISTED HOPPING

Sections S-5 to S-7 are devoted to the t - t_n - U Hubbard model—the nearest-neighbor Hubbard model augmented by a DAH term. They provide analytical details elucidating the origin of particle-hole asymmetry of our TaSK results for spectral quantities reported in the main text.

In this section, we compute the self-energy of the t - t_n - U Hubbard model up to second order in the interaction, i.e. $\mathcal{O}(U^2, Ut_n, t_n^2)$. The purpose of this analytical exercise is to gain an understanding of what kind of leading-order scattering processes lead to particle-hole asymmetry in the Hubbard model with DAH. Readers interested only in the numerical procedure can skip this section.

We consider the t - t_n - U Hamiltonian $H = H_t + H_U + H_n$,

$$H_t = -t \sum_{\langle ij \rangle, \sigma} (c_{i\sigma}^{\dagger} c_{j\sigma} + \text{h.c.}), \quad (\text{S46a})$$

$$H_U = U \sum_i n_{i\uparrow} n_{i\downarrow}, \quad (\text{S46b})$$

$$H_n = -t_n \sum_{\langle ij \rangle, \sigma} (c_{i\sigma}^{\dagger} c_{j\sigma} + \text{h.c.}) (n_{i\bar{\sigma}} + n_{j\bar{\sigma}}). \quad (\text{S46c})$$

We choose the chemical potential μ such that the ground state is half-filled and describes a paramagnetic state. Specifically, half-filling implies $\langle n_{\bar{\sigma}} \rangle = 1/2$ and, if t_n is treated within the Hartree-Fock approximation, $\mu = U/2$.

A. Hartree-Fock treatment

We begin our analysis by showing that a simple Hartree-Fock (HF) treatment is insufficient to yield particle-hole asymmetric features. The HF self-energy has the form

$$\Sigma_{\mathbf{k}}^{\text{HF}} = U \langle n_{\bar{\sigma}} \rangle - 4 \langle n_{\bar{\sigma}} \rangle t_n \gamma_{\mathbf{k}} \quad (\text{S47})$$

$$\gamma_{\mathbf{k}} = \cos k_x + \cos k_y. \quad (\text{S48})$$

At half-filling, the HF propagator has the form

$$\begin{aligned} G_{\mathbf{k}}^{\text{HF}}(\omega) &= \frac{1}{\omega^+ + \mu - \epsilon_{\mathbf{k}} - \Sigma_{\mathbf{k}}^{\text{HF}}}, \quad (\text{S49}) \\ &= \frac{1}{\omega^+ - \epsilon_{\mathbf{k}} - 2t_n \gamma_{\mathbf{k}}}, \end{aligned}$$

with $\omega^+ = \omega + i0^+$ and free dispersion $\epsilon_{\mathbf{k}} = -2t\gamma_{\mathbf{k}}$. $G_{\mathbf{k}}^{\text{HF}}(\omega)$ is particle-hole symmetric, with an effective nearest-neighbor single-particle hopping amplitude and dispersion

$$t_{\text{eff}} = t + t_n, \quad \epsilon_{\mathbf{k}}^{\text{eff}} = -2t_{\text{eff}} \gamma_{\mathbf{k}}. \quad (\text{S50})$$

Therefore, the significant particle-hole *asymmetries* cannot be explained by treating the DAH on the HF level. Even if the self-energy is computed to all orders in U , a

HF treatment of DAH would yield a particle-hole symmetric spectrum. Understanding the particle-hole asymmetry requires at least second-order perturbation theory, which we outline below.

B. Momentum space interaction vertices

Fourier transforming the interaction terms H_U and H_n in Eq. (S46) yields

$$H_x = \frac{1}{N} \sum_{\mathbf{k}, \mathbf{q}, \mathbf{p}, \sigma} V_{\mathbf{k}, \mathbf{q}}^x c_{\mathbf{k}+\mathbf{q}\sigma}^\dagger c_{\mathbf{k}\sigma} c_{\mathbf{p}-\mathbf{q}\bar{\sigma}}^\dagger c_{\mathbf{p}\bar{\sigma}}, \quad (\text{S51a})$$

$$V_{\mathbf{k}, \mathbf{q}}^U = U, \quad V_{\mathbf{k}, \mathbf{q}}^n = -2t_n [\gamma_{\mathbf{k}} + \gamma_{\mathbf{k}+\mathbf{q}}]. \quad (\text{S51b})$$

Hence, the total vertex entering second-order diagrams is

$$V_{\mathbf{k}, \mathbf{q}} = V_{\mathbf{k}, \mathbf{q}}^U + V_{\mathbf{k}, \mathbf{q}}^n = U - 2t_n [\gamma_{\mathbf{k}} + \gamma_{\mathbf{k}+\mathbf{q}}]. \quad (\text{S52})$$

C. Second-order self-energy

We now compute the second-order self-energy on top of the particle-hole symmetric HF solution. It is given by the usual ‘‘sunset’’ diagram, which describes an electron scattered by opposite-spin density fluctuations. On the Matsubara axis, this gives

$$\begin{aligned} \Sigma_{\mathbf{k}}^{(2)}(i\omega_m) &= \frac{1}{\beta N} \sum_{n\mathbf{q}} [V_{\mathbf{k}, \mathbf{q}}]^2 G_{\mathbf{k}+\mathbf{q}}^{\text{HF}}(i\omega_m + i\Omega_n) \Pi_{\mathbf{q}}^{\text{HF}}(i\Omega_n), \\ \Pi_{\mathbf{q}}^{\text{HF}}(i\Omega_n) &= -\frac{1}{\beta N} \sum_{n\mathbf{p}} G_{\mathbf{p}}^{\text{HF}}(i\nu_n) G_{\mathbf{p}+\mathbf{q}}^{\text{HF}}(i\nu_n + i\Omega_n). \end{aligned} \quad (\text{S53})$$

where $\Pi_{\mathbf{q}}^{\text{HF}}$ is a particle-hole bubble. Analytic continuation, $i\omega_m \rightarrow \omega^+$, yields the retarded real-frequency self-energy

$$\Sigma_{\mathbf{k}}^{(2)}(\omega) = \frac{4\pi^2}{N} \sum_{\mathbf{q}} [V_{\mathbf{k}, \mathbf{q}}]^2 \int_{-\infty}^{\infty} \frac{d\Omega}{2\pi} \int_{-\infty}^{\infty} \frac{d\omega'}{2\pi} \frac{A_{\mathbf{k}+\mathbf{q}}^{\text{HF}}(\omega') B_{\mathbf{q}}^{\text{HF}}(\Omega) [n_B(\Omega) + f(\omega')]}{\omega^+ - \omega' - \Omega}, \quad (\text{S54})$$

with Fermi-Dirac and Bose-Einstein distributions $f(x)$ and $n_B(x)$, respectively, and HF spectral functions

$$A_{\mathbf{k}}^{\text{HF}}(\omega) = \delta(\omega - \epsilon_{\mathbf{k}}^{\text{eff}}), \quad (\text{S55a})$$

$$\begin{aligned} B_{\mathbf{q}}^{\text{HF}}(\Omega) &= -\frac{1}{\pi} \text{Im} \Pi_{\mathbf{q}}^{\text{HF}}(\Omega) \\ &= \frac{1}{N} \sum_{\mathbf{p}} [f(\epsilon_{\mathbf{p}}^{\text{eff}}) - f(\epsilon_{\mathbf{p}+\mathbf{q}}^{\text{eff}})] \delta(\Omega + \epsilon_{\mathbf{p}}^{\text{eff}} - \epsilon_{\mathbf{p}+\mathbf{q}}^{\text{eff}}). \end{aligned} \quad (\text{S55b})$$

The spectral part of Eq. (S54) is given by

$$\begin{aligned} -\text{Im} \Sigma_{\mathbf{k}}^{(2)}(\omega) &= \frac{\pi}{N^2} \sum_{\mathbf{q}, \mathbf{p}} [V_{\mathbf{k}, \mathbf{q}}]^2 [f(\epsilon_{\mathbf{p}}^{\text{eff}}) - f(\epsilon_{\mathbf{p}+\mathbf{q}}^{\text{eff}})] \\ &\times [n_B(\epsilon_{\mathbf{p}+\mathbf{q}}^{\text{eff}} - \epsilon_{\mathbf{p}}^{\text{eff}}) + f(\epsilon_{\mathbf{k}+\mathbf{q}}^{\text{eff}})] \delta(\omega - \epsilon_{\mathbf{k}+\mathbf{q}}^{\text{eff}} - \epsilon_{\mathbf{p}+\mathbf{q}}^{\text{eff}} + \epsilon_{\mathbf{p}}^{\text{eff}}). \end{aligned} \quad (\text{S56})$$

D. Decomposition into U^2 , Ut_n , and t_n^2 , and origin of leading-order particle-hole asymmetries

To understand the origin of particle-hole asymmetries, we express the squared vertex Eq. (S52) as

$$[V_{\mathbf{k}, \mathbf{q}}]^2 = [V_{\mathbf{k}, \mathbf{q}}^U]^2 + 2V_{\mathbf{k}, \mathbf{q}}^U V_{\mathbf{k}, \mathbf{q}}^n + [V_{\mathbf{k}, \mathbf{q}}^n]^2, \quad (\text{S57a})$$

$$[V_{\mathbf{k}, \mathbf{q}}^U]^2 = U^2, \quad (\text{S57b})$$

$$2V_{\mathbf{k}, \mathbf{q}}^U V_{\mathbf{k}, \mathbf{q}}^n = -4Ut_n (\gamma_{\mathbf{k}} + \gamma_{\mathbf{k}+\mathbf{q}}), \quad (\text{S57c})$$

$$[V_{\mathbf{k}, \mathbf{q}}^n]^2 = 4t_n^2 (\gamma_{\mathbf{k}} + \gamma_{\mathbf{k}+\mathbf{q}})^2. \quad (\text{S57d})$$

This induces a decomposition of the 2nd-order self-energy,

$$\Sigma_{\mathbf{k}}^{(2)}(\omega) = \Sigma_{\mathbf{k}}^{U^2}(\omega) + \Sigma_{\mathbf{k}}^{Ut_n}(\omega) + \Sigma_{\mathbf{k}}^{t_n^2}(\omega), \quad (\text{S58})$$

obtained by replacing the square of the full vertex $[V_{\mathbf{k}, \mathbf{q}}]^2$ in Eq. (S54) by $[V_{\mathbf{k}, \mathbf{q}}^U]^2$, $2V_{\mathbf{k}, \mathbf{q}}^U V_{\mathbf{k}, \mathbf{q}}^n$ or $[V_{\mathbf{k}, \mathbf{q}}^n]^2$, respectively. Using $\gamma_{\mathbf{k}+\mathbf{\Pi}} = -\gamma_{\mathbf{k}}$, where $\mathbf{\Pi} = (\pi, \pi)$, one may verify that both $\Sigma_{\mathbf{k}}^{U^2}(\omega)$ and $\Sigma_{\mathbf{k}}^{t_n^2}(\omega)$ are particle-hole symmetric,

$$\Sigma_{\mathbf{k}}^{U^2}(\omega) = \Sigma_{\mathbf{k}+\mathbf{\Pi}}^{U^2}(-\omega), \quad \Sigma_{\mathbf{k}}^{t_n^2}(\omega) = \Sigma_{\mathbf{k}+\mathbf{\Pi}}^{t_n^2}(-\omega), \quad (\text{S59})$$

whereas $\Sigma_{\mathbf{k}}^{Ut_n}(\omega)$ is *not*.

A simpler and more intuitive way to see this is to check how the Hamiltonian Eq. (S46) behaves under particle-hole transformations. Both the single-particle hopping H_t and the Hubbard interaction (plus chemical potential) $H_U - U/2 \sum_{i\sigma} n_{i\sigma}$ are invariant under particle-hole transformations. However, the DAH term transforms as

$$\begin{aligned} H_n &\rightarrow -2t_n \sum_{\langle ij \rangle, \sigma} (c_{i\sigma}^\dagger c_{j\sigma} + \text{h.c.}) \\ &+ t_n \sum_{\langle ij \rangle, \sigma} (c_{i\sigma}^\dagger c_{j\sigma} + \text{h.c.}) (n_{i\bar{\sigma}} + n_{j\bar{\sigma}}), \end{aligned} \quad (\text{S60})$$

i.e. it becomes a single-particle hopping term with amplitude $-2t_n$ plus a DAH term with *opposite* sign. This sign flip means that the corresponding vertex flips sign under a particle-hole transformation, $V_{\mathbf{k}, \mathbf{q}}^n \rightarrow -V_{\mathbf{k}, \mathbf{q}}^n$. The single-particle hopping term ensures that the effective hopping amplitude in the HF propagator does not change under particle-hole transformations at half-filling:

$$t \rightarrow t^{\text{ph}} = t + 2t_n, \quad t_n \rightarrow t_n^{\text{ph}} = -t_n, \quad (\text{S61})$$

$$t_{\text{eff}} \rightarrow t^{\text{ph}} + t_n^{\text{ph}} = t + t_n = t_{\text{eff}}. \quad (\text{S62})$$

Thus, $G_{\mathbf{k}}^{\text{HF}}(\omega)$ is particle-hole symmetric, as stated before.

From that discussion, we immediately see that all diagrams (assuming expansion in terms of HF propagators, and not counting the vertices in HF diagrams) containing an even number of V_n vertices are particle-hole symmetric, while those with an odd number of V_n vertices are particle-hole *anti*-symmetric, for instance

$$\Sigma_{\mathbf{k}}^{Ut_n}(\omega) = -\Sigma_{\mathbf{k}+\mathbf{\Pi}}^{Ut_n}(-\omega). \quad (\text{S63})$$

At second order, the particle-hole asymmetry at half-filling thus arises via an ‘‘cooperative’’ t_n - U scattering event, where a particle-hole pair is emitted via H_n , followed by re-absorption via H_U , or vice versa.

S-6. APPROXIMATE SELF-ENERGY CORRECTION FROM DENSITY-ASSISTED HOPPING

Guided by Sec. S-5, we construct a simple DAH-induced correction to the self-energy starting from a known Hubbard-model solution. The idea is to replace one of the two Hubbard vertices in the Hubbard self-energy by the external-leg part of the DAH vertex to expose the origin of the particle-hole asymmetry introduced by t_n .

In Sec. S-5, we have seen that at the lowest order beyond Hartree-Fock, particle-hole asymmetry arises from mixed U - t_n scattering from the Hubbard interaction and DAH. However, second-order perturbation theory describes a Fermi liquid and is not able to capture the Mott physics of the half-filled Hubbard model. To make progress on DAH in the presence of Mott physics, we use the fact that (i) a full solution to the t_{eff} - U Hubbard model, which has single-particle hopping $t_{\text{eff}} = t + t_n$ but no DAH, is equivalent to (ii) a solution of the t - t_n - U Hubbard model with DAH treated in the HF approximation, while U is treated non-perturbatively to all orders.

However, approximation (ii) (HF-for- t_n plus all-orders-in- U) does not capture particle-hole asymmetry. To go beyond (ii), we return to (i), but now add to the self-energy a beyond-HF estimate of the effect of DAH. To this end, we first note that the full t - t_n - U self-energy can be expressed in terms of bare incoming and outgoing scattering vertices, contracted with a six-point propagator R [cf. Eq. (19) of Ref. 49],

$$\Sigma_{\mathbf{k}}(\omega) = \Sigma_{\mathbf{k}}^{\text{HF}} + V \circ R \circ V \quad (\text{S64})$$

$$V \circ R \circ V = \sum_{\mathbf{p}_1 \mathbf{q}_1 \mathbf{p}_2 \mathbf{q}_2} \begin{array}{c} \text{p}_1 \quad \text{p}_2 \\ \text{k} \quad \text{k} \\ \text{p}_1 - \mathbf{q}_1 \quad \text{p}_2 + \mathbf{q}_2 \\ \text{V}_{\mathbf{k}, \mathbf{q}_1} \quad \text{V}_{\mathbf{k} - \mathbf{q}_2, \mathbf{q}_2} \\ \text{R} \\ \text{k} + \mathbf{q}_1 \quad \text{k} - \mathbf{q}_2 \end{array} \quad (\text{S65})$$

Here, $V_{\mathbf{k}, \mathbf{q}} = V_{\mathbf{k}, \mathbf{q}}^U + V_{\mathbf{k}, \mathbf{q}}^n$ is the bare vertex of Eq. (S52). We now exploit the fact that we can evaluate Eq. (S65) for the t_{eff} - U Hubbard model using TaSK. Its vertex $V_{\mathbf{k}, \mathbf{q}}^U$ does not depend on the internal or external momenta, i.e.

$$V^U \circ R^{t_{\text{eff}}-U} \circ V^U = U^2 \sum_{\mathbf{p}_1 \mathbf{q}_1} \sum_{\mathbf{p}_2 \mathbf{q}_2} R_{\mathbf{k} \mathbf{p}_1 \mathbf{p}_2, \mathbf{q}_1 \mathbf{q}_2}^{t_{\text{eff}}-U}(\omega). \quad (\text{S66})$$

Further, the DAH vertex $V_{\mathbf{k}, \mathbf{q}}^n = -2t_n [\gamma_{\mathbf{k}} + \gamma_{\mathbf{k}+\mathbf{q}}]$ has a part that does not depend on the internal momenta, $\tilde{V}_{\mathbf{k}, \mathbf{q}}^n = -2t_n \gamma_{\mathbf{k}}$ (and the same is true for $V_{\mathbf{k}-\mathbf{q}, \mathbf{q}}$). We can therefore evaluate the cross terms involving \tilde{V}^n and V^U ,

$$\begin{aligned} \tilde{V}^n \circ R^{t_{\text{eff}}-U} \circ V^U &= V^U \circ R^{t_{\text{eff}}-U} \circ \tilde{V}^n \\ &= -2 \frac{t_n \gamma_{\mathbf{k}}}{U} V^U \circ R^{t_{\text{eff}}-U} \circ V^U, \end{aligned} \quad (\text{S67})$$

which captures some of the first-order-in- t_n/U corrections.

The corresponding correction term to the self-energy is

$$\delta \Sigma_{\mathbf{k}}(\omega) = -4 \frac{t_n \gamma_{\mathbf{k}}}{U} (\Sigma_{\mathbf{k}}^{t_{\text{eff}}-U}(\omega) - \Sigma_{\mathbf{k}}^{\text{HF}}). \quad (\text{S68})$$

This is Eq. (12) of the main text.

It should be acknowledged, though, that this expression is at best a rough estimate of the beyond-HF effects of DAH. We now discuss two aspects that it neglects.

First: There is no strict reason why we can ignore the $\propto \gamma_{\mathbf{k}+\mathbf{q}}$ momentum-transfer part of V_n . That said, we expect its contribution to be smaller than that of the $\propto \gamma_{\mathbf{k}}$ part, since $R^{t_{\text{eff}}-U}$ can be expected to become approximately local deep in a Mott insulator. (This statement is exact for a Hubbard atom, or for a Mott insulator described by dynamical mean-field theory.) If $R^{t_{\text{eff}}-U}$ is approximately local, it depends only weakly on the transfer momenta \mathbf{q}_1 and \mathbf{q}_2 , such that

$$R_{\mathbf{k} \mathbf{p}_1 \mathbf{p}_2, \mathbf{q}_1 \mathbf{q}_2}^{t_{\text{eff}}-U}(\omega) \simeq \bar{R}_{\mathbf{k} \mathbf{p}_1 \mathbf{p}_2}^{t_{\text{eff}}-U}(\omega) = \frac{1}{N^2} \sum_{\mathbf{q}_1 \mathbf{q}_2} R_{\mathbf{k} \mathbf{p}_1 \mathbf{p}_2, \mathbf{q}_1 \mathbf{q}_2}^{t_{\text{eff}}-U}(\omega). \quad (\text{S69})$$

As a result,

$$\sum_{\mathbf{q}_1 \mathbf{q}_2} \gamma_{\mathbf{k}+\mathbf{q}_1} R_{\mathbf{k} \mathbf{p}_1 \mathbf{p}_2, \mathbf{q}_1 \mathbf{q}_2}^{t_{\text{eff}}-U}(\omega) \simeq \sum_{\mathbf{q}_1} \gamma_{\mathbf{k}+\mathbf{q}_1} N \bar{R}_{\mathbf{k} \mathbf{p}_1 \mathbf{p}_2}^{t_{\text{eff}}-U}(\omega) = 0, \quad (\text{S70})$$

since $\sum_{\mathbf{q}_1} \gamma_{\mathbf{k}+\mathbf{q}_1} = 0$. However, since $\Sigma_{\mathbf{k}}^{t_{\text{eff}}-U}(\omega)$ is momentum-dependent, $R^{t_{\text{eff}}-U}$ is clearly not completely local, i.e. the above argument is not quantitative.

Second: There is also no strict reason why we should ignore first-order in t_n/U changes to R . Therefore, Eq. (S68) clearly neglects order t_n/U terms.

To summarize: we regard Eq. (S68) as a simplified approximation that is not quantitatively reliable, but which does give some insight into the origin of the particle-hole asymmetries we observe in a full, non-perturbative treatment of DAH using TaSK in the main text.

S-7. MODIFICATION OF THE MOTT POLE DISPERSION DUE TO DENSITY-ASSISTED HOPPING

In this section, we show that the self-energy pole dispersion of a Mott insulator in the presence of DAH contains terms that exceed the nearest-neighbor range of the DAH term itself. We accomplish this using a high-frequency expansion of the Green's function. We first review this expansion and the result of Ref. 50, which identified the connection between the Mott pole dispersion and the single-particle dispersion for the case of a t - U Hubbard model. Our approach, while close in spirit to that of Ref. 50, reveals that the pole dispersion can be thought of as the *effective dispersion of a dressed fermion* [66]. This dressed fermion is exactly local for a pure Hubbard interaction, and *becomes non-local in the presence of DAH*. This non-locality causes the range of the pole dispersion

to become larger in the presence of DAH.

Mott insulators have a pole in their self-energies that (in finite dimensions) is generically dispersive. Generally, the Green's function and self-energy can be written as

$$G_{\mathbf{k}}(z) = \frac{1}{z + \mu - \epsilon_{\mathbf{k}} - \Sigma_{\mathbf{k}}(z)}, \quad (\text{S71})$$

$$\Sigma_{\mathbf{k}}(z) = \Sigma_{\mathbf{k}}^{\text{HF}} + \frac{\Delta_{\mathbf{k}}}{z - \xi_{\mathbf{k}} - R_{\mathbf{k}}(z)}, \quad (\text{S72})$$

Here, $\epsilon_{\mathbf{k}}$ is the free dispersion and μ the chemical potential. The parameters $\Sigma_{\mathbf{k}}^{\text{HF}}$, $\Delta_{\mathbf{k}} \geq 0$ and $\xi_{\mathbf{k}}$ are fixed by equal-time correlators, and the residual function $R_{\mathbf{k}}(z)$ scales as $\mathcal{O}(z^{-1})$ for large $|z|$. $\xi_{\mathbf{k}}$ is the ‘‘dispersion of the self-energy pole’’.

Following the standard continued-fraction construction [52, 53], we define the interaction-dressed creation operator

$$\tilde{q}_{i\sigma}^{\dagger} = [H, c_{i\sigma}^{\dagger}] - \sum_j c_{j\sigma}^{\dagger} \langle \{c_{j\sigma}, [H, c_{i\sigma}^{\dagger}]\} \rangle, \quad (\text{S73a})$$

$$\begin{aligned} \tilde{q}_{\mathbf{k}\sigma}^{\dagger} &= \frac{1}{\sqrt{N}} \sum_j e^{-i\mathbf{k}\cdot\mathbf{r}_j} \tilde{q}_{j\sigma}^{\dagger} \\ &= [H, c_{\mathbf{k}\sigma}^{\dagger}] - c_{\mathbf{k}\sigma}^{\dagger} \langle \{c_{\mathbf{k}\sigma}, [H, c_{\mathbf{k}\sigma}^{\dagger}]\} \rangle. \end{aligned} \quad (\text{S73b})$$

By construction $\langle \{c_{\mathbf{k}\sigma}, \tilde{q}_{\mathbf{k}\sigma}^{\dagger}\} \rangle = 0$, i.e. $\tilde{q}_{\mathbf{k}\sigma}^{\dagger}$ is orthogonal to $c_{\mathbf{k}\sigma}^{\dagger}$ w.r.t. the operator scalar product $(A|B) = \langle \{A^{\dagger}, B\} \rangle$. We call operators orthogonal to single-particle operators ‘‘single-particle irreducible’’, since they determine the dynamical part of the self-energy [51, 52].

Using $E_{\mathbf{k}} \equiv \epsilon_{\mathbf{k}} + \Sigma_{\mathbf{k}}^{\text{HF}} - \mu$, we expand the Green's function, in powers of $1/z$:

$$\begin{aligned} G_{\mathbf{k}}(z) &= \frac{1}{z - E_{\mathbf{k}} - \frac{\Delta_{\mathbf{k}}}{z - \xi_{\mathbf{k}} - R_{\mathbf{k}}(z)}} = \frac{1}{z} \frac{1}{1 - \frac{E_{\mathbf{k}}}{z} - \frac{\Delta_{\mathbf{k}}}{z^2} - \frac{\Delta_{\mathbf{k}}\xi_{\mathbf{k}}}{z^3} + \mathcal{O}(z^{-4})}, \\ &= \frac{1}{z} + \frac{E_{\mathbf{k}}}{z^2} + \frac{E_{\mathbf{k}}^2 + \Delta_{\mathbf{k}}}{z^3} + \frac{E_{\mathbf{k}}^3 + 2E_{\mathbf{k}}\Delta_{\mathbf{k}} + \Delta_{\mathbf{k}}\xi_{\mathbf{k}}}{z^4} + \mathcal{O}(z^{-5}). \end{aligned} \quad (\text{S77})$$

The Green's function is fully determined by $E_{\mathbf{k}}$, $\Delta_{\mathbf{k}}$ and $\xi_{\mathbf{k}}$ up to order z^{-4} .

Alternatively, the high-frequency expansion can also be obtained from equations of motion for the retarded Green's function,

$$\begin{aligned} G_{\mathbf{k}}(t) &= -i\theta(t) \langle \{c_{\mathbf{k}\sigma}(t), c_{\mathbf{k}\sigma}^{\dagger}\} \rangle \\ &= -i\theta(t) \langle \{c_{\mathbf{k}\sigma}, c_{\mathbf{k}\sigma}^{\dagger}(-t)\} \rangle. \end{aligned} \quad (\text{S78})$$

For $\text{Im } z > 0$, we perform the high-frequency expansion of the integral

$$G_{\mathbf{k}}(z) = \int_0^{\infty} dt e^{izt} G_{\mathbf{k}}(t) = \sum_{n=0}^{\infty} \frac{\partial_t^n G_{\mathbf{k}}(t)|_{t=0^+}}{(iz)^{n+1}}, \quad (\text{S79})$$

The parameters $\Sigma_{\mathbf{k}}^{\text{HF}}$, $\Delta_{\mathbf{k}} \geq 0$ and $\xi_{\mathbf{k}}$ are given by

$$\Sigma_{\mathbf{k}}^{\text{HF}} + \epsilon_{\mathbf{k}} - \mu = \langle \{c_{\mathbf{k}\sigma}, [H, c_{\mathbf{k}\sigma}^{\dagger}]\} \rangle \quad (\text{S74a})$$

$$\Delta_{\mathbf{k}} = \langle \{\tilde{q}_{\mathbf{k}\sigma}, \tilde{q}_{\mathbf{k}\sigma}^{\dagger}\} \rangle, \quad (\text{S74b})$$

$$\xi_{\mathbf{k}}\Delta_{\mathbf{k}} = \langle \{\tilde{q}_{\mathbf{k}\sigma}, [H, \tilde{q}_{\mathbf{k}\sigma}^{\dagger}]\} \rangle. \quad (\text{S74c})$$

Equations (S74a) and (S74c) can be thought of as matrix-elements of the Liouvillian superoperator, defined as $\mathcal{L}O = [H, O]$, w.r.t. $c_{\mathbf{k}\sigma}^{\dagger}$ or $\tilde{q}_{\mathbf{k}\sigma}^{\dagger}$, respectively, while Eq. (S74b) is the norm of $\tilde{q}_{\mathbf{k}\sigma}^{\dagger}$.

The corresponding real-space versions are obtained via Fourier-transform,

$$\Delta_{ij} = \frac{1}{N} \sum_{\mathbf{k}} \Delta_{\mathbf{k}} e^{-i\mathbf{k}(\mathbf{r}_i - \mathbf{r}_j)} = \langle \{\tilde{q}_{i\sigma}, \tilde{q}_{j\sigma}^{\dagger}\} \rangle \quad (\text{S75a})$$

$$\begin{aligned} [\xi\Delta]_{ij} &= \sum_{\ell} \xi_{i\ell} \Delta_{\ell j} = \frac{1}{N} \sum_{\mathbf{k}} \xi_{\mathbf{k}} \Delta_{\mathbf{k}} e^{-i\mathbf{k}(\mathbf{r}_i - \mathbf{r}_j)} \\ &= \langle \{\tilde{q}_{i\sigma}, [H, \tilde{q}_{j\sigma}^{\dagger}]\} \rangle. \end{aligned} \quad (\text{S75b})$$

A. High-frequency expansion and identification of $\Delta_{\mathbf{k}}$ and $\xi_{\mathbf{k}}$

The formulas above can be obtained through a high-frequency expansion of the Green's function,

$$G_{\mathbf{k}}(z) = \frac{1}{z} \sum_{n=0}^{\infty} \frac{M_{\mathbf{k}}^{(n)}}{z^n}. \quad (\text{S76})$$

For our interests, we need this expansion up to and including $n = 3$.

which follows from repeated usage of

$$\int_0^{\infty} dt e^{izt} f(t) = \left[\frac{e^{izt}}{iz} f(t) \right]_{0^+}^{\infty} - \frac{1}{iz} \int_0^{\infty} dt e^{izt} \partial_t f(t). \quad (\text{S80})$$

The expansion coefficients can be written as equal-time correlation functions,

$$M_{\mathbf{k}}^{(n)} = (-i)^{n+1} \partial_t^n G_{\mathbf{k}}(t) \quad (\text{S81})$$

$$= (-1)^m \langle \{\mathcal{L}^m c_{\mathbf{k}}, \mathcal{L}^{n-m} c_{\mathbf{k}}^{\dagger}\} \rangle, \quad m \leq n,$$

with the Liouvillian $\mathcal{L}O = [H, O]$.

Comparing the expansion coefficients from Eqs (S77) and (S79), we find

$$M_{\mathbf{k}}^{(0)} = \langle \{c_{\mathbf{k}\sigma}, c_{\mathbf{k}\sigma}^{\dagger}\} \rangle = 1, \quad (\text{S82a})$$

$$M_{\mathbf{k}}^{(1)} = \langle \{c_{\mathbf{k}\sigma}, [H, c_{\mathbf{k}\sigma}^{\dagger}]\} \rangle = \langle \{[c_{\mathbf{k}\sigma}, H], c_{\mathbf{k}\sigma}^{\dagger}\} \rangle = E_{\mathbf{k}}, \quad (\text{S82b})$$

$$M_{\mathbf{k}}^{(2)} = \langle \{[c_{\mathbf{k}\sigma}, H], [H, c_{\mathbf{k}\sigma}^\dagger]\} \rangle = \langle \{\tilde{q}_{\mathbf{k}\sigma}, \tilde{q}_{\mathbf{k}\sigma}^\dagger\} \rangle + E_{\mathbf{k}}^2$$

$$= E_{\mathbf{k}}^2 + \Delta_{\mathbf{k}}, \quad (\text{S82c})$$

$$M_{\mathbf{k}}^{(3)} = \langle \{[c_{\mathbf{k}\sigma}, H], [H, [H, c_{\mathbf{k}\sigma}^\dagger]]\} \rangle$$

$$= \langle \{\tilde{q}_{\mathbf{k}\sigma} + E_{\mathbf{k}} c_{\mathbf{k}}, [H, \tilde{q}_{\mathbf{k}\sigma}^\dagger + E_{\mathbf{k}} c_{\mathbf{k}}^\dagger]\} \rangle$$

$$= \langle \{\tilde{q}_{\mathbf{k}\sigma}, [H, \tilde{q}_{\mathbf{k}\sigma}^\dagger]\} \rangle + E_{\mathbf{k}} \underbrace{\langle \{\tilde{q}_{\mathbf{k}\sigma}, [H, c_{\mathbf{k}}^\dagger]\} \rangle}_{=\Delta_{\mathbf{k}}}$$

$$+ E_{\mathbf{k}} \underbrace{\langle \{c_{\mathbf{k}}, [H, \tilde{q}_{\mathbf{k}\sigma}^\dagger]\} \rangle}_{=\Delta_{\mathbf{k}}} + E_{\mathbf{k}}^2 \langle \{c_{\mathbf{k}}, [H, c_{\mathbf{k}}^\dagger]\} \rangle$$

$$= E_{\mathbf{k}}^3 + 2E_{\mathbf{k}}\Delta_{\mathbf{k}} + \Delta_{\mathbf{k}}\xi_{\mathbf{k}}, \quad (\text{S82d})$$

where we used $\langle \{c_{\mathbf{k}\sigma}, \tilde{q}_{\mathbf{k}\sigma}^\dagger\} \rangle = 0$ to eliminate mixed terms and the relation $\langle \{A, [H, B]\} \rangle = \langle \{[A, H], B\} \rangle$, which follows from trace cyclicity. Equations (S74) directly follow from Eqs. (S82).

B. Pure Hubbard model (no DAH): local \tilde{q} and nearest-neighbor ξ

Consider now the Hamiltonian

$$H = \sum_{\sigma} T_{\sigma} + H_U \quad (\text{S83a})$$

$$H_U = U \sum_i n_{i\uparrow} n_{i\downarrow} - \mu \sum_{i\sigma} n_{i\sigma} \quad (\text{S83b})$$

$$T_{\sigma} = \sum_{ij} t_{ij} c_{i\sigma}^\dagger c_{j\sigma}, \quad (\text{S83c})$$

with chemical potential $\mu = U/2$, nearest-neighbor hopping t_{ij} , and therefore half-filling, $\langle n_{i\sigma} \rangle = \frac{1}{2}$ (assuming no ordering). Then, we find

$$[H, c_{i\sigma}^\dagger] = c_{i\sigma}^\dagger (U n_{i\bar{\sigma}} - \mu) + \sum_j t_{ji} c_{j\sigma}^\dagger \quad (\text{S84a})$$

$$\tilde{q}_{i\sigma}^\dagger = U c_{i\sigma}^\dagger \underbrace{(n_{i\bar{\sigma}} - \langle n_{i\bar{\sigma}} \rangle)}_{\equiv \delta n_{i\bar{\sigma}}}. \quad (\text{S84b})$$

At half-filling, $\langle n_{i\bar{\sigma}} \rangle = \frac{1}{2}$ and $(n_{i\bar{\sigma}} - \frac{1}{2})^2 = \frac{1}{4}$, hence

$$\Delta_{\mathbf{k}} = \langle \{\tilde{q}_{\mathbf{k}\sigma}, \tilde{q}_{\mathbf{k}\sigma}^\dagger\} \rangle = U^2 \langle (n_{i\bar{\sigma}} - \frac{1}{2})^2 \rangle = \frac{U^2}{4}. \quad (\text{S85})$$

To obtain $\xi_{\mathbf{k}}$, we compute

$$[H_U, \tilde{q}_{i\sigma}^\dagger] = U c_{i\sigma}^\dagger (U n_{i\bar{\sigma}} - \mu) \delta n_{i\bar{\sigma}} \quad (\text{S86a})$$

$$= U c_{i\sigma}^\dagger [(U - \mu - U \langle n_{i\bar{\sigma}} \rangle) n_{i\bar{\sigma}} + \mu \langle n_{i\bar{\sigma}} \rangle],$$

$$[T_{\bar{\sigma}}, \tilde{q}_{i\sigma}^\dagger] = U \sum_j t_{ji} c_{j\sigma}^\dagger \delta n_{i\bar{\sigma}}, \quad (\text{S86b})$$

$$[T_{\bar{\sigma}}, \tilde{q}_{i\sigma}^\dagger] = U c_{i\sigma}^\dagger [T_{\bar{\sigma}}, n_{i\bar{\sigma}}] = U c_{i\sigma}^\dagger X_{i\bar{\sigma}}, \quad (\text{S86c})$$

$$X_{i\bar{\sigma}} = [T_{\bar{\sigma}}, n_{i\bar{\sigma}}] \quad (\text{S86d})$$

$$= \sum_{\ell} (t_{i\ell} c_{i\bar{\sigma}}^\dagger c_{\ell\bar{\sigma}} - t_{\ell i} c_{\ell\bar{\sigma}}^\dagger c_{i\bar{\sigma}}).$$

Assuming particle-hole symmetry, the corresponding contributions are

$$\langle \{\tilde{q}_{j\sigma}, [H_U, \tilde{q}_{i\sigma}^\dagger]\} \rangle = \frac{U^2}{4} (U - \mu - U \langle n_{i\bar{\sigma}} \rangle) = 0, \quad (\text{S87a})$$

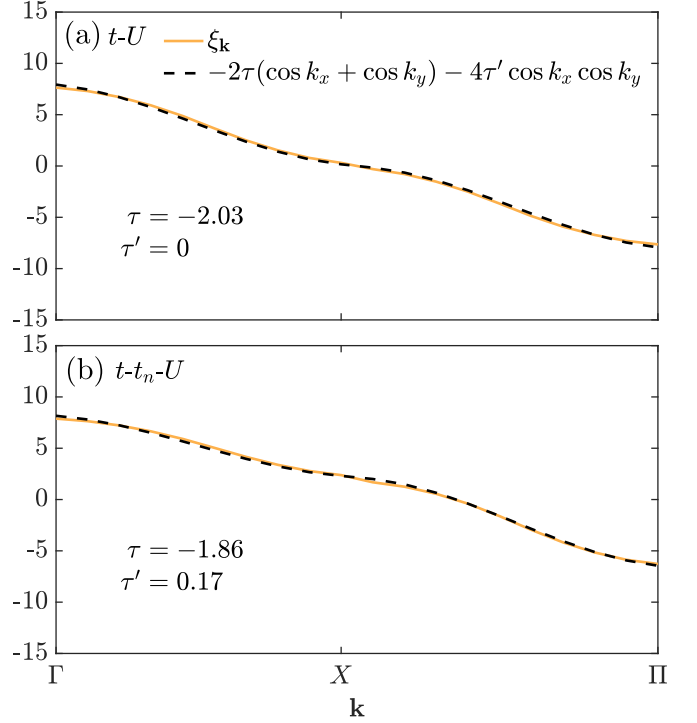


FIG. S-7. Self-energy pole dispersion $\xi_{\mathbf{k}}$ of (a) the t - U and (b) the t - t_n - U model, with parameters as in the main text. The solid orange line is obtained from TaSK, the black dashed line is a fit.

$$\langle \{\tilde{q}_{j\sigma}, [T_{\sigma}, \tilde{q}_{i\sigma}^\dagger]\} \rangle = U^2 t_{ji} \langle \delta n_{j\bar{\sigma}} \delta n_{i\bar{\sigma}} \rangle, \quad (\text{S87b})$$

$$\langle \{\tilde{q}_{j\sigma}, [T_{\bar{\sigma}}, \tilde{q}_{i\sigma}^\dagger]\} \rangle = U^2 \delta_{ij} \langle \delta n_{j\bar{\sigma}} X_{i\bar{\sigma}} \rangle \quad (\text{S87c})$$

$$+ U^2 \langle c_{i\sigma}^\dagger [X_{i\bar{\sigma}}, \delta n_{j\bar{\sigma}}] c_{j\sigma} \rangle.$$

The commutator in Eq. (S87c) evaluates to

$$[X_{i\bar{\sigma}}, \delta n_{j\bar{\sigma}}] = \sum_{\ell} (t_{\ell i} (\delta_{\ell j} - \delta_{ij}) c_{\ell\bar{\sigma}}^\dagger c_{i\bar{\sigma}} \quad (\text{S87d})$$

$$- t_{i\ell} (\delta_{ij} - \delta_{\ell j}) c_{i\bar{\sigma}}^\dagger c_{\ell\bar{\sigma}})$$

$$= \begin{cases} t_{ji} c_{j\bar{\sigma}}^\dagger c_{i\bar{\sigma}} + t_{ij} c_{i\bar{\sigma}}^\dagger c_{j\bar{\sigma}}, & j \neq i, \\ - \sum_{\ell} (t_{\ell i} c_{\ell\bar{\sigma}}^\dagger c_{i\bar{\sigma}} + t_{i\ell} c_{i\bar{\sigma}}^\dagger c_{\ell\bar{\sigma}}), & j = i. \end{cases}$$

Inserting this in Eq. (S87c), we get

$$\langle \{\tilde{q}_{j\sigma}, [T_{\bar{\sigma}}, \tilde{q}_{i\sigma}^\dagger]\} \rangle = \quad (\text{S87e})$$

$$U^2 \delta_{ij} \left[\sum_{\ell} (t_{\ell i} \langle \delta n_{i\bar{\sigma}} c_{\ell\bar{\sigma}}^\dagger c_{i\bar{\sigma}} \rangle - t_{i\ell} \langle \delta n_{i\bar{\sigma}} c_{i\bar{\sigma}}^\dagger c_{\ell\bar{\sigma}} \rangle) \right.$$

$$\left. - \sum_{\ell} (t_{\ell i} \langle n_{i\sigma} c_{\ell\bar{\sigma}}^\dagger c_{i\bar{\sigma}} \rangle + t_{i\ell} \langle n_{i\sigma} c_{i\bar{\sigma}}^\dagger c_{\ell\bar{\sigma}} \rangle) \right]$$

$$+ U^2 (\delta_{ij} - 1) [t_{ji} \langle c_{i\sigma}^\dagger c_{j\sigma} c_{j\bar{\sigma}}^\dagger c_{i\bar{\sigma}} \rangle + t_{ij} \langle c_{i\sigma}^\dagger c_{j\sigma} c_{i\bar{\sigma}}^\dagger c_{j\bar{\sigma}} \rangle].$$

Only Eqs. (S87b) and (S87c) generate non-local contributions. Since Δ in Eq. (S85) is \mathbf{k} -independent (local), $[\xi\Delta]_{ij} = \xi_{ij}\Delta$. Hence, for $i \neq j$,

$$\xi_{ij} = 4t_{ij} \left(\langle \delta n_{i\bar{\sigma}} \delta n_{j\bar{\sigma}} \rangle + \langle c_{i\sigma}^\dagger [X_{i\bar{\sigma}}, \delta n_{j\bar{\sigma}}] c_{j\sigma} \rangle \right), \quad (\text{S88})$$

so the pole dispersion inherits the range of the bare hopping: $\xi_{ij} \propto t_{ij}$ and vanishes when $t_{ij} = 0$, i.e. ξ_{ij} does

not exceed the range of the latter.

If the hopping t_{ij} is nearest-neighbor, we therefore expect

$$\xi_{\mathbf{k}} = -2\tau(\cos k_x + \cos k_y), \quad (\text{S89})$$

where τ is given by Eq. (S88) for i, j nearest-neighbors. We further expect $\tau < 0$ because of antiferromagnetic correlations [50]. Figure S-7(a) shows $\xi_{\mathbf{k}}$ (solid line) extracted from our discrete t - U data via continued fraction expansion, along the same momentum path as that taken in Fig. 3(a), together with a fit (dashed line) using the ansatz $-2\tau(\cos k_x + \cos k_y) - 4\tau' \cos k_x \cos k_y$, with τ' a possible next-nearest neighbor amplitude. We find $\tau = -2.03 < 0$ and, as expected, $\tau' = 0$.

C. Adding density-assisted hopping: nonlocal \tilde{q} and emergent next-nearest neighbor term in $\xi_{\mathbf{k}}$

We now augment the Hubbard model with a DAH term,

$$T_{n\sigma} = \sum_{ij} t_{ij}^n c_{i\sigma}^\dagger c_{j\sigma} (n_{i\bar{\sigma}} + n_{j\bar{\sigma}}). \quad (\text{S90})$$

The \tilde{q} operator acquires additional contributions from DAH,

$$[T_{n\sigma}, c_{i\sigma}^\dagger] = \sum_j t_{ji}^n c_{j\sigma}^\dagger (n_{i\bar{\sigma}} + n_{j\bar{\sigma}}) \quad (\text{S91})$$

$$[T_{n\bar{\sigma}}, c_{i\sigma}^\dagger] = \sum_j t_{ji}^n (c_{j\bar{\sigma}}^\dagger c_{i\bar{\sigma}} + \text{h.c.}) c_{i\sigma}^\dagger \quad (\text{S92})$$

$$\begin{aligned} \tilde{q}_{i\sigma}^\dagger &= U c_{i\sigma}^\dagger \delta n_{i\bar{\sigma}} + \sum_j t_{ji}^n c_{j\sigma}^\dagger (\delta n_{i\bar{\sigma}} + \delta n_{j\bar{\sigma}}) \quad (\text{S93}) \\ &+ \sum_j t_{ji}^n (c_{j\bar{\sigma}}^\dagger c_{i\bar{\sigma}} - \langle c_{j\bar{\sigma}}^\dagger c_{i\bar{\sigma}} \rangle + \text{h.c.}) c_{i\sigma}^\dagger. \end{aligned}$$

Equation (S93) shows that $\tilde{q}_{i\sigma}^\dagger$ becomes *nonlocal* in the presence of DAH: (i) a creation operator $c_{j\sigma}^\dagger$ on site j

multiplied by a density operator $\delta n_{i\bar{\sigma}}$ at site i , and (ii) an intersite spin-exchange term $(c_{j\bar{\sigma}}^\dagger c_{i\bar{\sigma}} + \text{h.c.}) c_{i\sigma}^\dagger$.

The non-local nature of $\tilde{q}_{i\sigma}^\dagger$ results in non-local contributions to Δ that are of order t^n/U ,

$$\Delta_{ij} = \frac{U^2}{4} (\delta_{ij} + \mathcal{O}(t^n/U)). \quad (\text{S94})$$

To isolate the key effects on the range of ξ , we focus on the large local part of Δ in the discussion below. Taking into account its non-locality would reinforce the conclusions.

Crucially, the non-locality of $\tilde{q}_{i\sigma}^\dagger$ produces contributions to $[\xi\Delta]_{ij}$ (and therefore also ξ_{ij}) that extend beyond the range of either t_{ij} or t_{ij}^n . The spatial range of $[\xi\Delta]_{ij}$ is determined by (i) the range of $\tilde{q}_{i\sigma}^\dagger$ and (ii) how the Liouvillian $\mathcal{L} = [H, \bullet]$ acts to “move” fermionic operators—through either the single-particle hopping or the DAH process, whichever is longer-ranged (both are nearest-neighbor in the present case). Consequently, ξ_{ij} acquires terms proportional to $t_{i\ell}^n t_{\ell j}$; unlike in the t - U model, *the range of ξ exceeds the range of t* .

For the t - t_n - U model studied in the main text, where both t and t_n are nearest-neighbor, we expect that ξ_{ij} contains *next*-nearest neighbor terms. As for the t - U model, we extract the pole dispersion $\xi_{\mathbf{k}}$ via a continued fraction expansion of the discrete spectral function, and fit it with the ansatz

$$\xi_{\mathbf{k}} = -2\tau(\cos k_x + \cos k_y) - 4\tau' \cos k_x \cos k_y. \quad (\text{S95})$$

The result of this is shown in Fig. S-7(b), and we find $\tau = -1.86$ and $\tau' = 0.17$, i.e. the next-nearest neighbor term τ' is indeed sizeable. We have also tried including a next-to-next nearest neighbor term $-2\tau''(\cos 2k_x + \cos 2k_y)$ (not shown). We find that $\tau'' = 0.05$, while τ and τ' are unaffected.